Neurobiology of Aging 136 (2024) 157–170

Contents lists available at ScienceDirect

Neurobiology of Aging

journal homepage: www.elsevier.com/locate/neuaging.org

Brain structural indicators of β-amyloid neuropathology

Ikbeom Jang [a,b,c,*], Binyin Li [d], Barnaly Rashid [a,e], John Jacoby [a,b], Susie Y. Huang [a,b,f], Bradford C. Dickerson [a,e,g], David H. Salat [a,b,h], for the Alzheimer's Disease Neuroimaging Initiative

[a] Athinoula A. Martinos Center for Biomedical Imaging, Massachusetts General Hospital, Charlestown, MA, USA
[b] Department of Radiology, Harvard Medical School, Boston, MA, USA
[c] Division of Computer Engineering, Hankuk University of Foreign Studies, Yongin, South Korea
[d] Department of Neurology, Ruijin Hospital, Shanghai Jiao Tong University School of Medicine, Shanghai, China
[e] Department of Neurology, Harvard Medical School, Boston, MA, USA
[f] Harvard-MIT Division of Health Sciences and Technology, Massachusetts Institute of Technology, Cambridge, MA, USA
[g] Department of Psychiatry, Harvard Medical School, Boston, MA, USA
[h] Neuroimaging Research for Veterans Center, VA Boston Healthcare System, Boston, MA, USA

ARTICLE INFO

Keywords:
Alzheimer's disease
Amyloid beta neuropathology
Gray matter to white matter contrast
Machine learning
MRI
PET

ABSTRACT

Recent efforts demonstrated the efficacy of identifying early-stage neuropathology of Alzheimer's disease (AD) through lumbar puncture cerebrospinal fluid assessment and positron emission tomography (PET) radiotracer imaging. These methods are effective yet are invasive, expensive, and not widely accessible. We extend and improve the multiscale structural mapping (MSSM) procedure to develop structural indicators of β-amyloid neuropathology in preclinical AD, by capturing both macrostructural and microstructural properties throughout the cerebral cortex using a structural MRI. We find that the MSSM signal is regionally altered in clear positive and negative cases of preclinical amyloid pathology (N = 220) when cortical thickness alone or hippocampal volume is not. It exhibits widespread effects of amyloid positivity across the posterior temporal, parietal, and medial prefrontal cortex, surprisingly consistent with the typical pattern of amyloid deposition. The MSSM signal is significantly correlated with amyloid PET in almost half of the cortex, much of which overlaps with regions where beta-amyloid accumulates, suggesting it could provide a regional brain 'map' that is not available from systemic markers such as plasma markers.

1. Introduction

Alzheimer's disease (AD) is defined histopathologically by amyloid and tau neuropathology (Bateman et al., 2012; Buchhave et al., 2012; Jack et al., 2012). This pathology begins a decade or more prior to the onset of clinical symptoms. (Bateman et al., 2012; Buchhave et al., 2012; Jack et al., 2013, 2012, 2010; Landau et al., 2012; Michelle M. Mielke et al., 2012). Clinically symptomatic identification of AD is therefore late in the process and at a time when novel therapeutics will be less effective. Thus, identification of early pathology has been a goal for the development of novel biomarker techniques. The recent biological framework of AD emphasizes three types of pathology to characterize this disorder, referred to as the 'amyloid/tau/neurodegeneration' (A-T-N) framework. The primary validated measures of amyloid and tau neuropathology include lumbar puncture cerebrospinal fluid (CSF) assessment and positron emission tomography (PET) using radiotracers for the abnormal proteins. Their routine use for screening is limited due to their invasiveness, high costs, and the requirement for specialized facilities. Blood-based biochemical markers such as plasma markers are emerging and becoming available, however, they still require validation and are invasive. In contrast, structural brain imaging with MRI is commonly performed to assess for gross pathology that can contribute to cognitive impairment, e.g., brain tumors, intracranial hemorrhage, and sequela of prior traumatic injury or vascular disease. Combined with machine learning approaches, brain MRI can successfully identify individuals with Alzheimer's disease or mild cognitive impairment (MCI) (Allison et al., 2019; Belathur Suresh et al., 2018; Cho et al., 2012; Choi et al., 2020; Davatzikos et al., 2008; Desikan et al., 2009; Gao et al.,

* Correspondence to: Athinoula A. Martinos Center for Biomedical Imaging, MGH Department of Radiology, Building 149, 13th Street Mail Code 149(2301), Charlestown, MA 02129, United States.
E-mail address: ikbeom.jang@mgh.harvard.edu (I. Jang).

https://doi.org/10.1016/j.neurobiolaging.2024.01.005
Received 19 July 2023; Received in revised form 10 January 2024; Accepted 13 January 2024
Available online 18 January 2024

2020; Janghel and Rathore, 2021; H.T. Li et al., 2021; Lin et al., 2018; Lu et al., 2018; Magnin et al., 2009; Park et al., 2017; Popuri et al., 2020; Sørensen et al., 2017; Suk et al., 2014; Westman et al., 2012; Wolz et al., 2011; Zhang et al., 2011). However, structural brain imaging is limited in detecting AD at its earliest stages and is particularly challenged in the preclinical/asymptomatic stages. To date, few studies have used structural imaging robustly in the detection of primary markers of AD pathology in cognitively intact individuals (Ten Kate et al., 2018; Tosun et al., 2021).

While macrostructural morphometry procedures such as cortical thickness/volume, hippocampal volume, and gray matter volumes are commonly used in structural MRI studies, microstructural properties are also quantifiable from a standard structural T1-weighted MR image yet are not widely utilized (Jang et al., 2022; Jefferson et al., 2015; Salat et al., 2011, 2009). In a prior study, we integrated morphometry measures with image signal properties to develop a novel multiscale MRI procedure that allows quantification of features at both macrostructural and microstructural scales throughout the cerebral cortex from a single structural MRI scan to quantify brain tissue integrity across multiple spatial scales (referred to as 'multi-scale structural mapping'; MSSM) (Jang et al., 2022). The procedure exhibited enhanced ability for detecting degeneration in Alzheimer's disease and mild cognitive impairment compared to traditional measures such as cortical thickness and hippocampal volume, suggesting that MSSM provides a sensitive measure of Alzheimer's disease neurodegeneration. We find that the MSSM-based procedure serves as a sensitive indicator of preclinical amyloid pathology and that the MSSM signal is regionally altered in clear positive and negative cases of preclinical amyloid pathology when cortical thickness alone or hippocampal volume is not. This procedure could therefore provide a regional brain 'map' that is not available from systemic markers such as plasma and CSF biomarkers. Thus, this procedure may provide a metric for the 'A′ component as well as the 'N′ of the 'A-T-N′ biological framework for AD. These novel procedures We propose here a MSSM-based procedure to predict amyloid beta (Aβ) status in cognitively unimpaired, healthy individuals, as such procedures could be clinically feasible in future implementations. To validate our procedure's ability to detect amyloid positivity in asymptomatic individuals, we compared its performance against traditional morphometry metrics such as cortical thickness and hippocampal volume. may have applications in determining appropriate candidates for clinical trials to test novel therapeutics that would ameliorate Alzheimer's disease pathologies.

2. Materials and methods

2.1. Participants

Data were obtained from the ADNI GO, 2, and 3 databases (http://adni.loni.usc.edu) for 467 participants. Non-impaired participants with accelerated 3-D T1-weighted MRI and amyloid measure – florbetapir PET or β-amyloid (1−42) in CSF – were included. There were 190 cognitively unimpaired (CU) participants who were amyloid-β (Aβ) positive ($A\beta^{+}_{PET-CSF}$; age=71.5 ± 6.2) and 277 age/sex/education-matched CU participants who were Aβ negative ($A\beta^{-}_{PET-CSF}$; age=72.6 ± 6.0). Note that cognitive scores were also matched as a result suggesting that $A\beta^{+}_{PET-CSF}$ were not close to impairment. The matching was validated by both the *t*-test and the Kolmogorov-Smirnov test. The ADNI diagnosis criteria were made based on the National Institute of Neurological Disorders and Stroke and the Alzheimer's Disease and Related Disorders Association. The inclusion criteria for CU participants were an absence of significant impairment in cognitive functions or activities of daily living, Clinical Dementia Rating (CDR) of 0, free of memory complaints, and haven't been diagnosed with AD or MCI. The criteria for amyloid positivity are described below in the "Beta-amyloid measurement" section. The cohort selection procedure did not involve any manual intervention, and random sampling was used whenever applicable (Fig. 1). Demographic, clinical, and cognitive characteristics of the analyzed participants are provided in Table 1. Since this study is a 'proof of concept' to show the effectiveness of the MSSM procedure, we limited this investigation to the ADNI databases (ADNI GO, 2, and 3 cohorts).

2.2. MRI acquisition

Brain images were acquired with accelerated 3D isotropic T1-weighted parallel imaging using 3 T MRI scanners – either magnetization-prepared rapid gradient-echo (MP-RAGE) or fast spoiled gradient-echo (FSPGR) – and multi-channel coils. Data were collected from 62 imaging sites using one of 15 MRI scanner models manufactured by Siemens, GE, or Philips. MR Imaging followed the ADNI protocols. Imaging parameters varied, with the most common parameters being TR= 2300 ms, TE=min full echo (e.g., 2.98 ms), flip angle= 9°, voxel size= $1 \times 1 \times 1.2\ mm^3$. Data from the participants' initial visit were used. If Florbetapir PET was not available at the initial visit, data at a later session that has it was used. We prioritized accelerated scans – i.e., undersampled k-space for reduced scan time – aligning with our goal of developing cost-effective biomarkers. The MR images were reconstructed using Sensitivity Encoding for Fast MRI (SENSE) or Generalized Autocalibrating Partially Parallel Acquisition (GRAPPA) at the scanner.

2.3. Beta-amyloid measurement

Amyloid data were collected using either PET imaging or CSF samples ($A\beta_{PET\text{-}CSF;}$ N = 467). CSF data were used for those with both PET and CSF. As a result, CSF data of 293 participants and PET data of the other 174 participants were used to measure beta-amyloid in analyses. Amyloid-β 1 to 42 peptide ($A\beta_{1-42}$) was measured in CSF in the morning after an overnight fast during their baseline visit. Lumbar puncture was performed with a 20- or 24-gauge spinal needle as described in the ADNI procedures manual (https://adni.loni.usc.edu/methods/documents/). Amyloid PET data were collected from 62 imaging sites using one of 19 PET scanner models manufactured by GE, Philips, or CTI (sold as Siemens). ^{18}F-Florbetapir PET images were obtained and pre-processed with a protocol described in http://adni.loni.usc.edu/methods/pet-analysis-method/pet-analysis/. In brief, dynamic 3D scans of four 5-minute frames were acquired 50–70 min after the injection of the fluorine-labeled tracer, florbetapir (370 MBq; 10 mCi). Separate frames were co-registered with one another to reduce the effects of motion and then all frames were averaged. Each averaged PET image was reoriented into a standard space, intensity-normalized, and spatially smoothed to have an 8 mm isotropic resolution. Data were then processed at the Jagust lab at the University of California, Berkeley, as described in previous studies (Landau et al., 2013b). Each PET image was co-registered to the corresponding MRI, and the mean florbetapir uptake within the cortical and reference regions was computed. The average Florbetapir whole brain standardized uptake value ratio (SUVR) was calculated by averaging across the four cortical regions and dividing this summary ROI by the uptake in the whole cerebellum. The first available data was used for each participant if data were available in multiple sessions. We used amyloid cutoffs that are commonly used in the literature – i.e., CSF cutoff of 836 pg/mL and PET SUVR cutoff of 1.13 – although they vary by study (Bucci et al., 2021; Camus et al., 2012; Dumurgier et al., 2015; Ezzati et al., 2020; Fleisher et al., 2011; Hansson et al., 2018; Landau et al., 2013a; Sturchio et al., 2021; Tosun et al., 2021).

2.4. Multiscale structural mapping (MSSM) signal extraction

The MSSM procedure is summarized in Fig. 2. First, image processing followed the standard FreeSurfer reconstruction procedure as described in prior work (Dale et al., 1999; Fischl et al., 2004, 2002, 1999a, 1999b; Fischl and Dale, 2000; Salat et al., 2011; Ségonne et al., 2004) using the

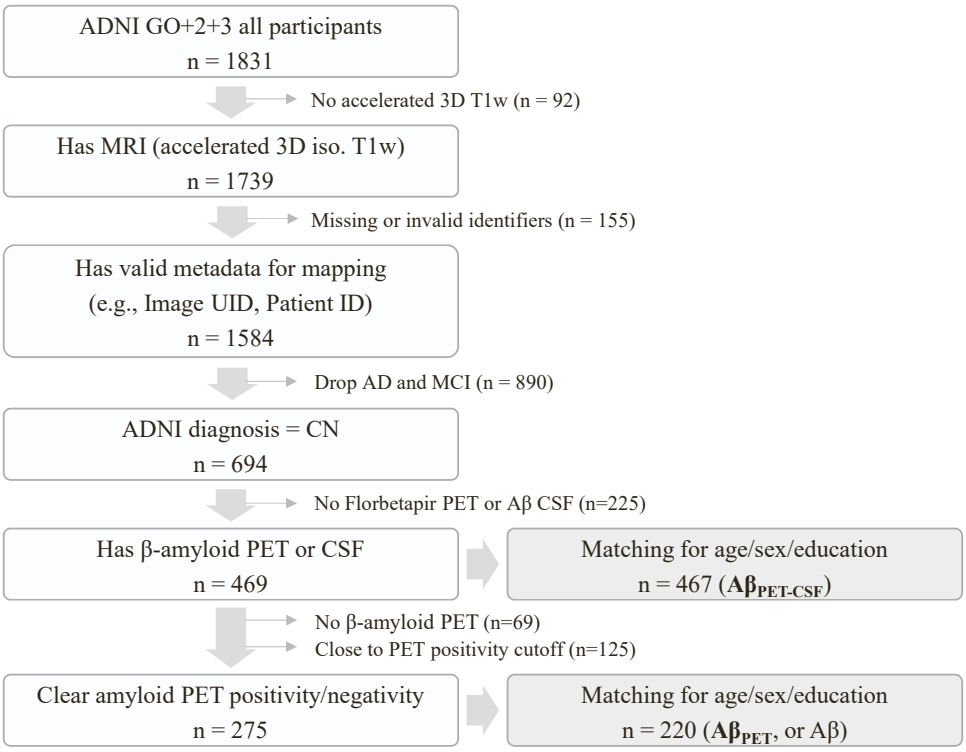

Fig. 1. Diagram of cohort selection.

Table 1
Participants' demographic, clinical, and cognitive characteristics in the PET-CSF-combined dataset ($A\beta_{PET\text{-}CSF}$). Only data used for the analyses are included in the table. The two groups are matched for age, gender, education, and cognitive performance. $A\beta^{+}_{PET-CSF}$, amyloid positive validated by PET or CSF; $A\beta^{-}_{PET-CSF}$, amyloid negative validated by PET or CSF; $^{*}p < 0.05$.

	$A\beta^{+}_{PET-CSF}$	$A\beta^{-}_{PET-CSF}$
Number of participants	190	277
Age (year)	71.5 ± 6.2	72.6 ± 6.0
Gender (female/male)	116 / 74	156 / 121
Education (year)	16.6 ± 2.3	16.5 ± 2.7
Proportion of non-Hispanic white	79.5%	85.6%
ADNI Diagnosis	CN	CN
Aβ CSF (ABETA; N = 293)	661 ± 203*	1546 ± 433
Aβ PET (AV45; N = 174)	1.3 ± 0.2*	1.0 ± 0.1
CDR-SB	0.1 ± 0.2	0.0 ± 0.2
MMSE	29.0 ± 1.3	29.0 ± 1.2
MoCA	26.1 ± 2.4	25.9 ± 2.5
FAQ	0.2 ± 0.6	0.3 ± 1.3
RAVLT Immediate	45.6 ± 10.1	47.2 ± 10.2
RAVLT Percent forgetting	31.4 ± 34.0	34.1 ± 28.3
ADAS-Cog 11	5.3 ± 2.7	5.5 ± 2.9
ADAS-Cog 13	8.4 ± 4.2	8.5 ± 4.2

FreeSurfer image analysis suite v7.2 (http://surfer.nmr.mgh.harvard.edu)(Dale et al., 1999; Fischl et al., 2004, 2002, 1999a, 1999b; Fischl and Dale, 2000; Ségonne et al., 2004) (Fig. 2, panel a). To summarize, brain segmentation and cortical surface modeling were performed. The resulting cortical model provides us with the border between gray matter (GM) and white matter (WM) and the border between GM and CSF. We performed a series of deformable processes and computed morphometric features such as cortical thickness and curvature throughout the 3D cortical map. Second, multiple layers of cortical GM tissue signal properties were obtained. This is done by extracting the signal in the interior of the cortical ribbon at different depths between the GM/WM border (i.e., white surface) and the GM/CSF border (i.e., pial surface). We obtained 4 GM surfaces through cortical thickness – GM20%, GM40%, GM60%, GM80% – where GM20% being closest to GM/WM border (Fig. 2, panel b). Third, multiple layers of subcortical WM intensities were measured to provide localized normalization of GM tissue properties in the next step. We obtained 2 WM surfaces by sampling at 0.5 mm and 1.0 mm subjacent to the white surface (WM 0.5 mm and WM 1.0 mm; Fig. 2, panel b). Fig. 3 illustrates these procedures. Fourth, the intensity ratio between each pair of GM and WM signals (GWR) was computed at each cortical surface vertex. The term "vertex" means the smallest resolution element on a 3D mesh representation and is comparable to a "voxel" in a 3D image. The rationale for computing GWR is that the GM and WM intensities from neighboring voxels are expected to be similarly influenced by imaging parameters and protocols. Therefore, ratios between WM values and the corresponding GM values provide a (relatively) normalized unit across different imaging environments. 8 GWR maps were obtained by pairing 4 GMs and 2 WMs (Fig. 2, panel c). This multilayer sampling enables quantification at various contrast levels, from lower contrast near the GM/WM border (GM20%/WM 0.5 mm) to higher contrast between outer GM and deep WM (GM80%/WM 1.0 mm). Sixth, the GWR maps of each participant were registered to the standard fsaverage space and spatially smoothed with a Gaussian kernel of 5 mm full width at half maximum (FWHM) utilizing surface-based smoothing. Finally, these microscale feature maps were integrated with macroscale morphometric features (here, we used a cortical thickness map) for the full feature set (Fig. 2, panel d). The resulting vertex-wise measurements correspond to the fsaverage cortical mesh representation (~300,000 vertices both hemispheres). Vertex-wise partial least squares (PLS) discriminant analysis procedure is described in the next section.

2.5. Multivariable analysis & amyloid-β positivity detection

2.5.1. Train-test split

Data of $A\beta^{+}_{PET}$ and $A\beta^{-}_{PET}$ were randomly split into 80% training and 20% test sets while sampling an equal number of samples for each class to prevent biases in prediction. It is critical that the train-test split is done at the very beginning of all the procedures before data pre-

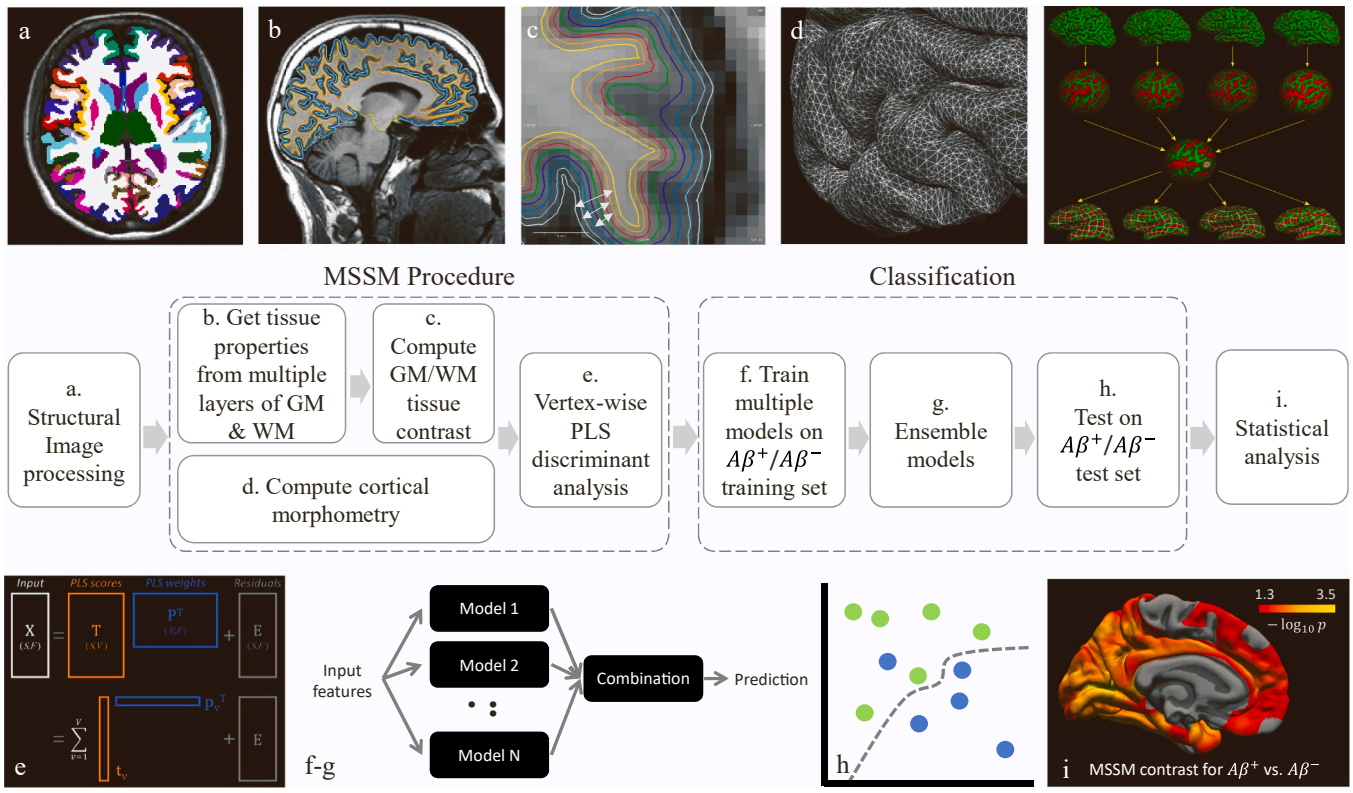

Fig. 2. Flowchart of the proposed MSSM procedure and classification. GM, gray matter; WM, white matter; PLS, partial least squares; $A\beta^+$, cognitively unimpaired participants with amyloid positivity; $A\beta^-$, cognitively unimpaired participants with amyloid negativity.

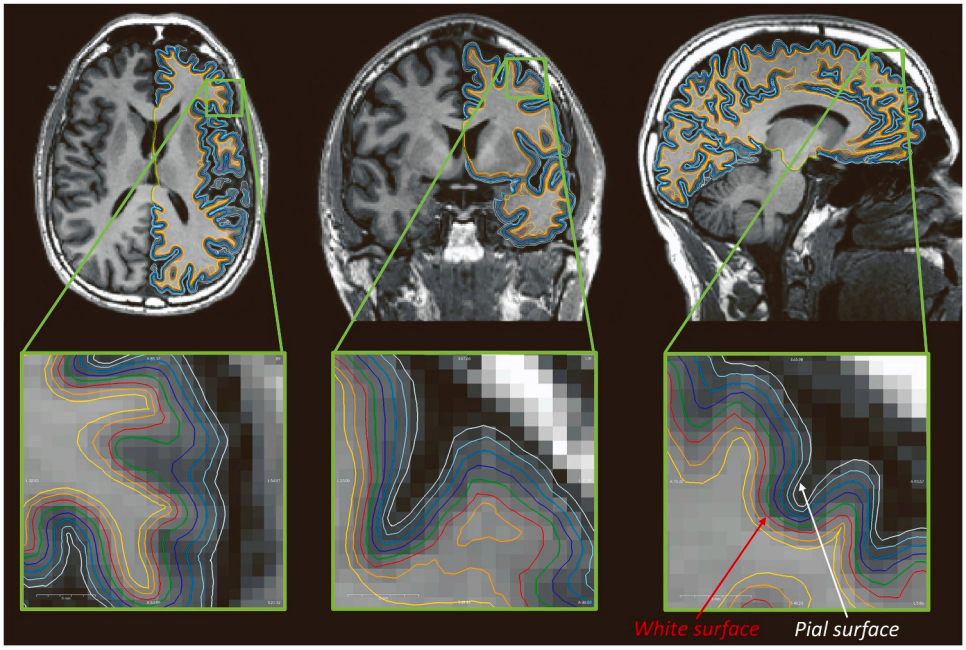

Fig. 3. Microstructural feature map generation using a structural T1-weighted image. We expanded the intensity/contrast metrics (GWR) to include tissue sampling from multiple points through the thickness of the cortical ribbon and subjacent white matter to obtain an array of intensity-linked features.

processing, feature extraction, and PLS. This allows the test set to be completely held out and never seen by any data processing or modeling. The training set was again split into training and validation sets, thereby having 70% training, 10% validation, and 20% test sets. The following procedures for feature extraction and model training were performed using the training and validation sets, and the test set was accessed strictly after the final model was established and trained.

2.5.2. *Feature selection*

The 8 gray/white matter contrasts and cortical thickness were used as primary features in the identification of individuals with $A\beta^+_{PET}$ and differentiation from matched controls with $A\beta^-_{PET}$.

2.5.3. Vertex-wise PLS regression

Each feature was normalized to have intensities between 0 and 1. Since we have more variables than observations and multicollinearity exists between the features, PLS regression (or PLS discriminant analysis in our problem) was used for dimensionality reduction for each vertex. The PLS method is used to find the direction in the feature space that explains the maximum variance direction in the Aβ label space (i.e., $A\beta^{+}_{PET}$ or $A\beta^{-}_{PET}$). The reduced feature map (one component per vertex) was used to train classification models (Fig. 2, panel e). We used the nonlinear iterative partial least squares (NIPALS) algorithm. See §A.1. for detailed description.

2.5.4. Model training

Multiple commonly used machine learning models were trained and optimized independently and ensembled in the end for final decision-making. Models considered in the study are support vector machines with varying kernels (linear, sigmoid, polynomial, radial basis function), neural networks, random forest, logistic regression, k-nearest neighbors, and Gaussian process classifiers. Hyperparameters of each model were optimized with a grid search. Class labels were binarized, and the probability of each class was estimated to enable analyses of the receiver operating characteristic (ROC) and precision-recall (PR) curve. We trained these models while accounting for the class imbalance when necessary. The validation set was used to find hyperparameters that maximize the classification performance. To improve our prior implementation (Jang et al., 2022) and mitigate overfitting, we optimized the number of vertices to be fed into the models as opposed to using all the vertices on the cortical surface. We first analyzed the effects of Aβ positivity on MSSM using standard statistical contrast (i.e., *t*-test) and only used vertices with a *p*-value lower than a certain threshold. The optimal threshold was found with a grid search (Fig. 2, panel f).

2.5.5. Ensemble learning

We randomly initialized and trained each model five times and identified three models with the highest average performance in the validation set. The primary performance measure we used is the area under the ROC curve (AUROC). 4-fold cross-validation was used to measure the average AUROC for each weight initialization, thereby having 20 AUROC values to be averaged for each model. The top 3 models were ensembled to form a single classifier, which makes a final decision (Fig. 2, panel g).

2.5.6. Evaluation

The inference was performed on the test set. All procedures described above were repeated five times using different random seeds for dataset split to provide performance statistics. The reported performance metrics are AUROC, the area under the PR curve (AUPRC), accuracy, sensitivity, specificity, and precision (Fig. 2, panel h).

2.6. Added value of MSSM

In the classification experiments, to examine the added value of the MSSM features, we performed an ablation study by comparing the performance of MSSM-based models with GWR-based models and cortical thickness-based models. For this, the same procedure described in the section above was performed with the cortical thickness map alone and GWR features alone, respectively. In case of cortical thickness, the vertex-wise PLS regression was not needed. Note that not only cortical thickness but also MSSM and GWRs have one feature per vertex since they went through dimensionality reduction with PLS. The performance of models using normalized hippocampal volume (normalized with estimated total intracranial volume (eTIV)) and models based on cognitive composite scores (e.g., MoCA, MMSE, RAVLT, ADAS) were also measured. Lastly, we examined whether adding demographic features—i.e., age, gender, education, race, and ethnicity—to MSSM helps in diagnostic performance.

Statistical analyses were performed as follows. We estimated the effect of global Aβ positivity on MSSM using standard statistical contrast—i.e., per-vertex group comparison between $A\beta^{+}_{PET}$ and $A\beta^{+}_{PET}$. Per-vertex *p*-value and effect size were reported on pial surface maps (called significance map and effect size map). After a cluster-based correction for multiple comparisons using a threshold of 0.05, only the surviving vertices were colored on the significance maps. The effect size was measured using Cohen's *d*. The effect of global Aβ positivity were also estimated for cortical thickness using the same sample to examine the added value of the MSSM features. The same was done for Aβ PET images (AV45) to show spatial pattern of amyloid deposition in non-diagnosed asymptomatic sample. Lastly, we analyzed the correlation between the regional SUVR values in Aβ-PET and the corresponding regional MSSM signal using a per-vertex Pearson's correlation analysis. When visualizing statistical effects on the cortical surface, FWHM of 20 mm was used throughout the paper to get images with less noise because we are interested in identifying affected ROIs rather than a few vertices (voxels). The Desikan-Killiany atlas was used as reference.

2.7. Analysis with PET-validated data only

We replicated the analyses with a subset of the dataset, exclusively employing PET data to establish a ground truth for amyloid positivity, considering notable discrepancies between PET and CSF measurements. Non-impaired participants with accelerated 3-D T1 and florbetapir PET scans were included in this analysis ($A\beta_{PET;}$ N = 220). There were 90 cognitively unimpaired (CU) participants who were amyloid-β (Aβ) positive ($A\beta^{+}_{PET}$; age=74.7 ± 6.3) and 130 age/sex/education-matched CU participants who were Aβ negative ($A\beta^{-}_{PET}$; age=73.5 ± 5.9). Note that cognitive scores were also matched as a result. The matching was validated by both the *t*-test and the Kolmogorov-Smirnov test. Acknowledging that many participants are around the amyloid positivity cutoff, we grouped participants into clearly positive and clearly negative groups via a data-driven procedure which determines optimal cutoffs and buffer for amyloid positivity. See §A.2. for detailed methods. Amyloid positivity criteria considerably vary by study, and our buffer range encompassed all cutoff thresholds identified in the relevant literature, ensuring a comprehensive representation of amyloid positivity, including Camus et al. (2012); Ezzati et al. (2020); Fleisher et al. (2011); Landau et al. (2013a); Tosun et al. (2021). The cohort selection procedure did not involve any manual intervention, and random sampling was used whenever applicable (Fig. 1). Demographic, clinical, and cognitive characteristics of the analyzed participants are provided in Table 2.

2.8. Statistical analysis

All statistical analyses, including hypothesis testing and correction for multiple comparisons, were conducted using FreeSurfer v7.2 tools (e.g., mri_glmfit, mri_glmfit-sim) or Python 3.7 (Python Software Foundation, https://www.python.org/psf/) and its libraries SciPy and statsmodels. Specific statistical methodologies used for each analysis are described within each subsection of the Materials and Methods. For comparisons across two groups, a student's *t*-test was performed as default. The Shapiro-Wilk test for normality was conducted to ensure the validity of using a *t*-test. If the assumption was violated, the non-parametric Mann-Whitney U test was used. Differences in the mean were considered statistically significant at $p < 0.05$, and the cluster correction was used whenever we did multiple comparisons throughout the cortical surface.

2.9. Data and code availability

Data used in the preparation of this article are publicly accessible

Table 2
Participants' demographic, clinical, and cognitive characteristics in the $A\beta_{PET}$ dataset. Only data used for the analyses are included in the table. The two groups are matched for age, gender, education, and cognitive performance. CN, cognitively normal participants; $A\beta_{PET}$, global amyloid-β level based on PET imaging (also called AV45 in ADNI); CDR-SB, Clinical Dementia Rating Sum of Boxes; MMSE, Mini-Mental State Exam; MoCA, Montreal Cognitive Assessment; FAQ, Functional Activities Questionnaire; RAVLT, Rey Auditory Verbal Learning Test; ADAS-Cog 11, Alzheimer's Disease Assessment Scale 11 cognitive items; ADAS-Cog 13, ADAS-Cog 11 plus a delayed recall task and the Digit Symbol Substitution Test. $^*p < 0.05$.

	$A\beta^+_{PET}$	$A\beta^-_{PET}$
Number of participants	90	130
Age (year)	74.7 ± 6.3	73.5 ± 5.9
Gender (female/male)	64 / 26	82 / 48
Education (year)	16.6 ± 2.3	16.8 ± 2.5
Proportion of non-Hispanic white	88.9%	87.7%
ADNI Diagnosis	CN	CN
Aβ PET (AV45)	1.4 ± 0.2*	1.0 ± 0.0
CDR-SB	0.1 ± 0.2	0.1 ± 0.2
MMSE	28.9 ± 1.3	29.0 ± 1.3
MoCA	25.4 ± 2.8	26.0 ± 2.5
FAQ	0.3 ± 0.6	0.3 ± 1.5
RAVLT Immediate	45.3 ± 10.5	46.1 ± 10.2
RAVLT Percent forgetting	37.0 ± 23.4	32.9 ± 37.0
ADAS-Cog 11	6.0 ± 3.0	5.4 ± 2.8
ADAS-Cog 13	9.4 ± 4.5	8.6 ± 4.4

from the Alzheimer's Disease Neuroimaging Initiative (ADNI) database (adni.loni.usc.edu). As such, the investigators within the ADNI contributed to the design and implementation of ADNI and/or provided data but did not participate in the analysis or writing of this report. A complete listing of ADNI investigators can be found at http://adni.loni.usc.edu/wp-content/uploads/how_to_apply/ADNI_Acknowledgement_List.pdf. Source codes for the method described in this paper are publicly available at https://github.com/jibikbam/MSSM.

3. Results

3.1. Added value of MSSM

We examined the added value of the MSSM features over traditional morphometry measured by cortical thickness alone in standard statistical group comparisons of Aβ+ to Aβ– participants. In standard statistical group comparisons for the full sample ($A\beta_{PET-CSF}$; N = 467), employing MSSM features resulted in a modest elevation in the count of statistically significant vertices differentiating the $A\beta^+_{PET-CSF}$ participants from $A\beta^-_{PET-CSF}$ compared with the cortical thickness features. Nevertheless, both methods detected effects in a minority of the cortical surface, with significant findings in fewer than 7% of total vertices. When using the PET-only dataset comprising clearly positive or negative cases, $A\beta_{PET}$ (N = 220), use of the MSSM features markedly increased the number of significant vertices differentiating the $A\beta^+_{PET}$ participants from $A\beta^-_{PET}$ compared to cortical thickness. 72.7% of the total vertices were significant for MSSM (Fig. 4A) compared to 8.6% significant with cortical thickness alone (Fig. 4E). MSSM demonstrated heightened sensitivity to a wide range of regions in the posterior temporal and parietal as well as medial prefrontal cortices. Specifically, these regions included the cingulate, precuneus, superior/middle-frontal gyrus, insula, fusiform gyrus, and superior/inferior parietal lobe. The left hemisphere showed spatially broader effect than in the right – 78.6% vs. 66.8% of the total vertices in each hemisphere (Fig. 4A). The significant regions exhibited a range of effect sizes from 0.25 to 0.60 (Fig. 4B). Many of these regions showing effects on MSSM overlapped with regions where beta-amyloid accumulates in our sample (Figs. 4C, 4D).

Analysis revealed that 45.4% of the total vertices exhibited significant correlations between regional SUVR values in Aβ-PET and the MSSM signal (Fig. 4F). Subsequent analyses focused more on the $A\beta_{PET}$ dataset due to its more pronounced effects compared to the modest findings in the PET-CSF-combined dataset.

We examined the most critical feature in differentiating amyloid positive and negative cases at each vertex within the PLS analysis. Among the nine features (8 GWR features and cortical thickness), GM 60%/WM 1.0 mm was the most important feature in 35% of the vertices, GM 80%/WM 1.0 mm in 19% of the vertices, and GM 80%/WM 0.5 mm in 12%. Cortical thickness accounted for 11%. Considering all contrast metrics together, it comprised 89% of the total significant vertices (Fig. 5). Looking at the second most important feature in each vertex, GM 80%/WM 1.0 mm comprised 21% of the total vertices, and GM60%/WM 0.5 mm 20%, whereas cortical thickness accounted for 2% (Fig. S1).

3.2. MSSM-based amyloid-β positivity detection

In predicting amyloid-β positivity among CU individuals, the MSSM features differentiated $A\beta^+_{PET-CSF}$ from $A\beta^-_{PET-CSF}$ with the area under the ROC curve (AUROC), the area under the PR curve (AUPRC), accuracy, sensitivity, specificity, and precision of 0.69, 0.67, 0.68, 0.63, 0.73, and 0.69 on average, respectively. The MSSM performance was significantly greater than conventional measures used in Alzheimer's studies – i.e., cortical thickness map, hippocampal volume, and clinical/cognitive scores as well as than the GWR-based model. Listing the models in order of performance is as follows: MSSM > GWR > Hippocampal volume > Cortical thickness > Cognitive scores. The performance values were 0.67, 0.62, 0.68, 0.48, 0.82, and 0.64 when GWRs were used, and 0.52, 0.50, 0.55, 0.47, 0.63, and 0.54 when cortical thickness was used, and 0.57, 0.56, 0.58, 0.77, 0.43, and 0.55 when hippocampal volume was used (Table 3). For the classification of $A\beta^+_{PET}$ vs. $A\beta^-_{PET}$ using the PET-only dataset, AUROC, AUPRC, accuracy, sensitivity, specificity, and precision of 0.70, 0.74, 0.71, 0.61, 0.80, and 0.78 on average, respectively. The performance was significantly better than conventional measures used in Alzheimer's studies – i.e., cortical thickness map, hippocampal volume, and clinical/cognitive scores as well as than the GWR-based model. Listing the models in order of performance is as follows: MSSM > GWR > Cortical thickness ~= Hippocampal volume > Cognitive scores. The performance values were 0.67, 0.68, 0.68, 0.73, 0.64, and 0.67 when GWRs were used, and 0.54, 0.56, 0.57, 0.46, 0.68, and 0.62 when cortical thickness was used, and 0.53, 0.57, 0.58, 0.37, 0.74, and 0.63 when hippocampal volume was used (Table 4). Random forests were most frequently selected in the ensemble followed by neural networks, support vector machine, and logistic regression. Inclusion of demographic variables did not enhance MSSM performance in either dataset.

We advanced the original MSSM procedure by introducing a process of selecting the vertices to be fed into the models based on the statistical contrast and optimizing the significance level (equivalent to optimizing/reducing the number of vertices to be fed). This improved the test performance significantly – i.e., a 5.7% increase in accuracy on average for $A\beta^+_{PET}$ vs. $A\beta^-_{PET}$. The training performance often reached 90–100% accuracy without this step; however, the performance gap between the training and test data was significantly reduced by adding this step, suggesting reduced overfitting. The classification performance on the $A\beta_{PET}$ test set is summarized in Table 4. In most cases, cognitive score-based models predicted everyone positive or everyone negative, presumably due to the fact that the groups were extremely matched. Thus, we omitted reporting the accuracy, sensitivity, specificity, and precision for these models, as they tended towards 0 or 1. The provided accuracy, sensitivity, specificity, and precision in the table are based on a decision threshold chosen to minimize the number of false detection (false positives plus false negatives). Decision thresholds can be adjusted to increase either sensitivity or specificity at the cost of the other.

Post-hoc analyses of misclassified individuals were performed on one of the training/testing rounds in the $A\beta_{PET}$ dataset to identify potential

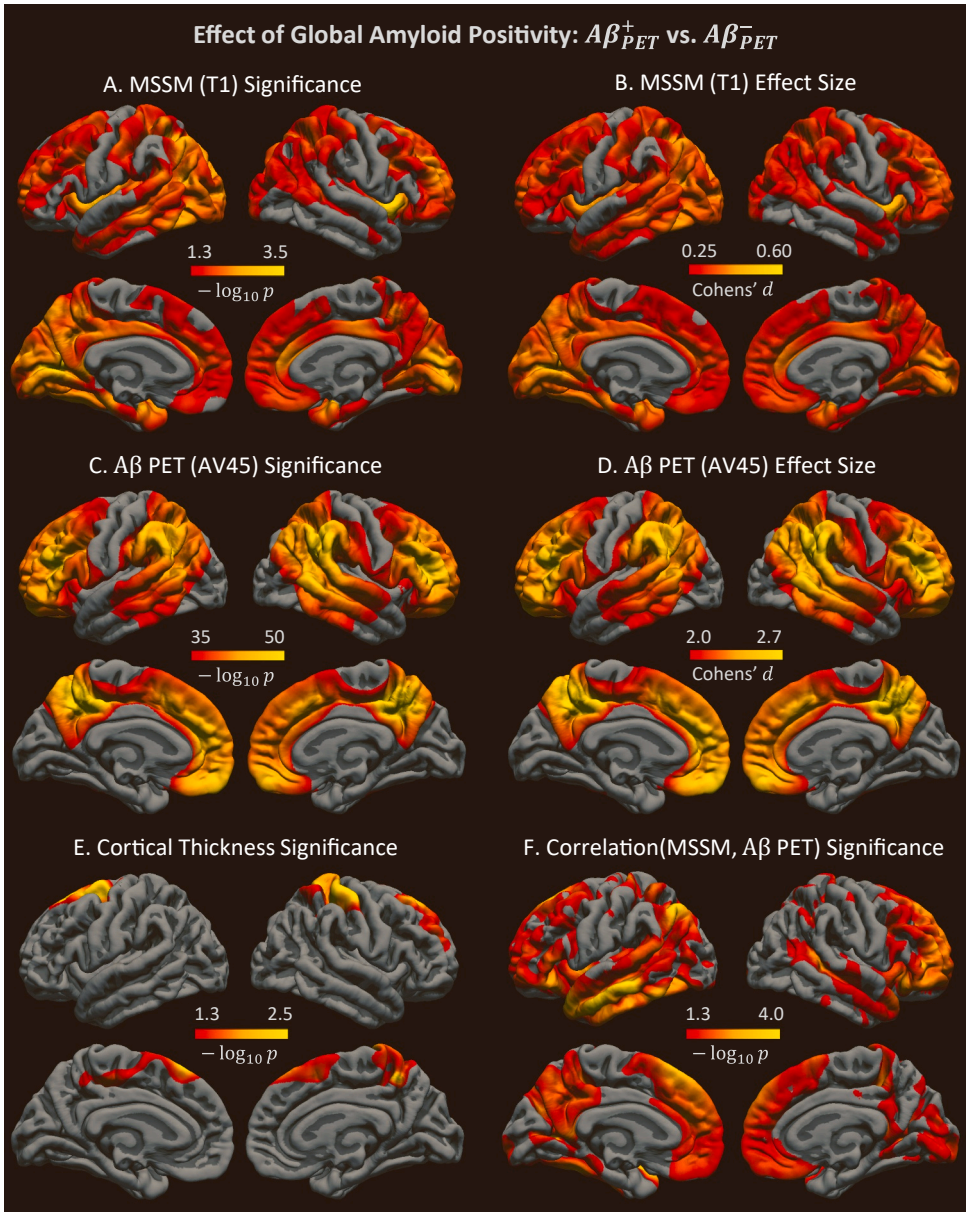

Fig. 4. Effects of global amyloid-β positivity on MSSM validated by PET. Standard statistical contrast in clearly + or – amyloid cases was used. MSSM features exhibited significant group differences between $A\beta^{+}_{PET}$ and $A\beta^{-}_{PET}$ across a substantial proportion of brain regions (72.7%) (A) while traditional cortical thickness map did not show differences in most of the regions in the same sample (8.6%) (E). Widespread effects were found with MSSM across the posterior temporal and parietal as well as medial prefrontal cortex, consistent with the contrast of amyloid PET (C) and typical patterns of Aβ deposition (Buckner et al., 2005; Gonzalez-Escamilla et al., 2021). The left hemisphere exhibited more extensive effects compared to the right. We quantified effect sizes for MSSM (B) and Aβ PET (D), represented by Cohen's *d* to assess the magnitude of differences. Correlation between the regional SUVR values in Aβ PET and the corresponding regional MSSM signal is shown (F). Significant associations were found in 45.4% of the total vertices. Cluster correction was used for multiple comparisons and only the surviving vertices were colored in the significance plots. Note that not only cortical thickness but also MSSM has one feature per vertex since it went through dimensionality reduction with PLS discriminant analysis.

causes of misclassification (25% misclassification in the test sample) other than potential errors caused by merging PET and CSF for amyloid ground truth and potential mislabels for those around the amyloid positivity cutoff. It revealed that the misclassified participants were statistically different from the mean of the correctly classified participants in multiple biomarkers and characteristics. The analyses included both training and testing data to have a larger sample size in statistical tests. Abbreviations are used to reduce verbosity as below:

- mAβ+ : misclassified Aβ+ participants (false negative, PET=Aβ+, model prediction=Aβ–)
- cAβ+ : correctly classified Aβ+ participants (true positive, PET=Aβ+, model prediction=Aβ+)
- mAβ–: misclassified Aβ– participants (false positive, PET=Aβ–, model prediction=Aβ+)
- cAβ–: correctly classified Aβ– (true negative, PET=Aβ–, model prediction=Aβ–)

First, the majority of the misclassified individuals, both mAβ+ and Aβ–, were 77 years old or older. mAβ– were older than cAβ– ($p < 0.05$) and were closer to cAβ+ in its mean and median. The volume of the entorhinal cortex in mAβ– was lower than that in cAβ– ($p < 0.05$) and was closer to cAβ+ . The volume of ventricles in mAβ+ was lower than

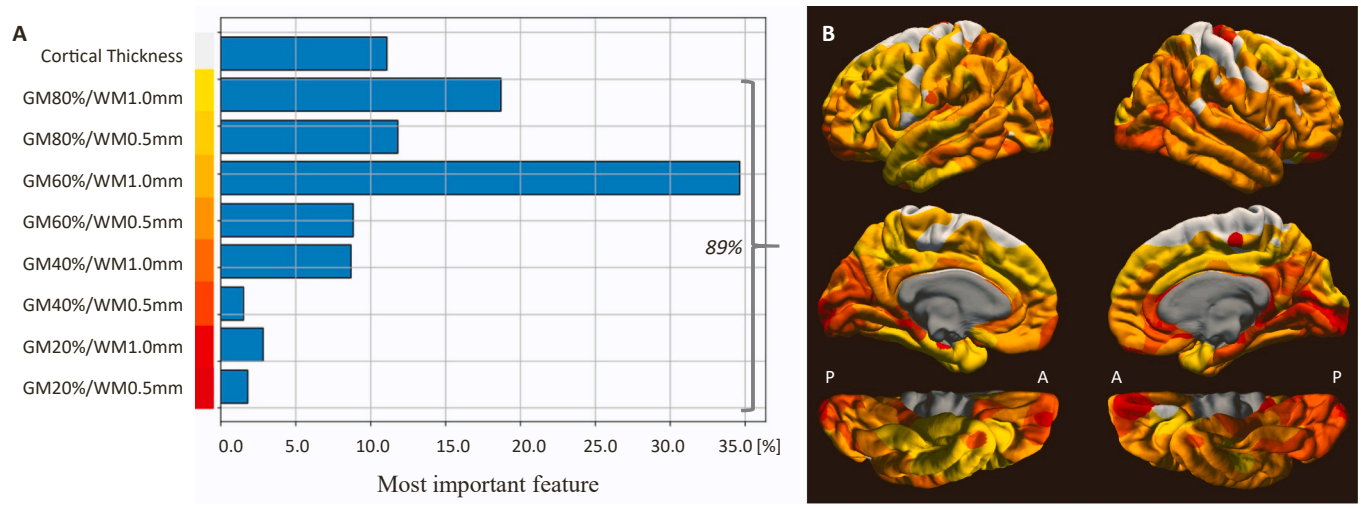

Fig. 5. Feature importance map. The most important feature at each vertex for differentiating $A\beta^{+}_{PET}$ individuals from $A\beta^{-}_{PET}$ in the PLS analysis. The bar chart shows how spatially dominant each of the MSSM features is over the cerebral cortex (A). The color-coded brain map shows the most important feature among the nine at each vertex (B).

Table 3
Performance in detecting amyloid positivity within cognitively intact individuals using the PET-CSF-combined dataset ($A\beta_{PET\text{-}CSF}$). The performance metrics of MSSM were compared to the models based on GWR, standard morphometry, and cognitive scores $^{*}p < 0.05$.

Features		AUROC	AUPRC	Accuracy	Sensitivity	Specificity	Precision
Cognitive Score-Based	CDR-SB	0.50 ± 0.03*	0.43 ± 0.06*				
	MMSE	0.52 ± 0.06*	0.43 ± 0.08*				
	MoCA	0.50 ± 0.05*	0.43 ± 0.07*				
	FAQ	0.52 ± 0.04*	0.43 ± 0.06*				
	RAVLT Immediate	0.56 ± 0.06*	0.49 ± 0.11*				
	RAVLT Percent forgetting	0.50 ± 0.08*	0.43 ± 0.10*				
	ADAS-Cog 11	0.56 ± 0.05*	0.45 ± 0.06*				
	ADAS-Cog 13	0.52 ± 0.04*	0.43 ± 0.08*				
Hippocampal Volume		0.57 ± 0.06*	0.56 ± 0.05*	0.58 ± 0.03*	0.77 ± 0.29*	0.43 ± 0.20*	0.55 ± 0.15*
Cortical Thickness		0.52 ± 0.09*	0.50 ± 0.06*	0.55 ± 0.05*	0.47 ± 0.43*	0.63 ± 0.40*	0.54 ± 0.28*
GWR		0.67 ± 0.08	0.62 ± 0.07*	0.68 ± 0.02	0.48 ± 0.19*	0.82 ± 0.13	0.64 ± 0.16
MSSM		0.69 ± 0.08	0.67 ± 0.09	0.68 ± 0.02	0.63 ± 0.11	0.73 ± 0.13	0.69 ± 0.07

Table 4
Performance in detecting amyloid positivity within cognitively intact individuals using the PET dataset ($\mathbf{A\beta_{PET}}$). The performance metrics of MSSM were compared to the models based on GWR, standard morphometry, and cognitive scores $^{*}p < 0.05$.

Features		AUROC	AUPRC	Accuracy	Sensitivity	Specificity	Precision
Cognitive Score-Based	CDR-SB	0.48 ± 0.00*	0.50 ± 0.02*				
	MMSE	0.55 ± 0.03*	0.55 ± 0.02*				
	MoCA	0.48 ± 0.04*	0.56 ± 0.04*				
	FAQ	0.54 ± 0.01*	0.54 ± 0.06*				
	RAVLT Immediate	0.60 ± 0.08*	0.62 ± 0.06*				
	RAVLT Percent forgetting	0.53 ± 0.01*	0.52 ± 0.03*				
	ADAS-Cog 11	0.57 ± 0.02*	0.55 ± 0.00*				
	ADAS-Cog 13	0.60 ± 0.02*	0.61 ± 0.09*				
Hippocampal Volume		0.53 ± 0.02*	0.57 ± 0.03*	0.58 ± 0.03*	0.37 ± 0.26*	0.74 ± 0.25	0.63 ± 0.13*
Cortical Thickness		0.54 ± 0.06*	0.56 ± 0.03*	0.57 ± 0.01*	0.46 ± 0.20*	0.68 ± 0.21*	0.62 ± 0.08*
GWR		0.67 ± 0.06	0.68 ± 0.05*	0.68 ± 0.01*	0.73 ± 0.17*	0.64 ± 0.20*	0.67 ± 0.08*
MSSM		0.70 ± 0.07	0.74 ± 0.08	0.71 ± 0.01	0.61 ± 0.10	0.80 ± 0.10	0.78 ± 0.06

cAβ+ ($p < 0.05$). The volume of each brain region was corrected for estimated total intracranial volume (eTIV), presented as a percentage of eTIV. mAβ+ had significantly smaller SUVR for ^{18}F-fluorodeoxyglucose (FDG) PET compared to cAβ+ ($p < 0.005$). Discrepancies were still observed in amyloid status between CSF β-amyloid$_{1–42}$ and PET Aβ, despite stratifying the sample using a wide buffer around PET Aβ thresholds. For example, amyloid status for a mAβ+ with 1336 pg/mL CSF Aβ was negative based on the CSF measure but positive with PET. Phosphorylated tau in CSF (CSF p-tau) for mAβ– was closer to cAβ+ than cAβ–. There are a few missing data points due to data unavailability (Fig. 6). Overall, misclassified (amyloid + or -) were older than correctly classified, had reduced FDG, greater CSF tau pathology and in the mAB- had larger ventricles and reduced volume compared to the correctly classified.

4. Discussion

This research holds crucial value by enabling neuropathological traits to be characterized through structural imaging features. Our results demonstrate alterations in tissue signal properties in the amyloid-

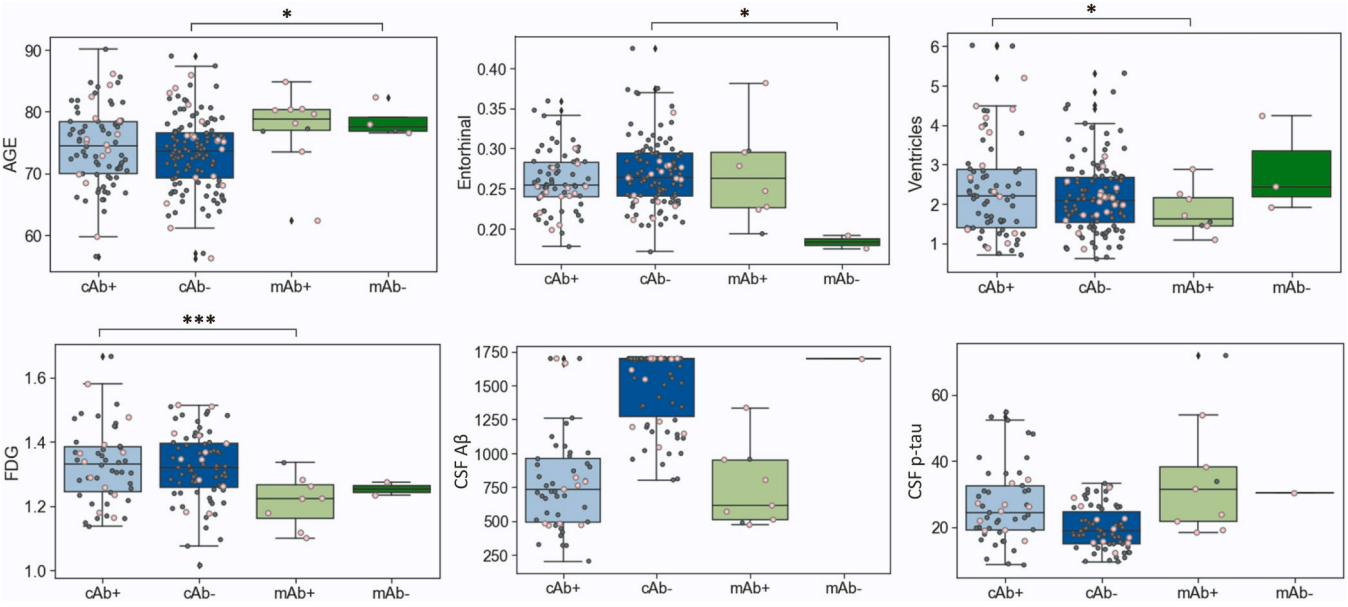

Fig. 6. Biomarkers of misclassified individuals in the detection of amyloid-β positivity within cognitively unimpaired participants in the $\mathbf{A\beta_{PET}}$ dataset. Volumes of the entorhinal cortex and ventricles were corrected for estimated total intracranial volume (eTIV), presented as a percentage of eTIV. Individuals in the test set are represented as a pink circle, and those in the training and validation sets are represented as dark gray. Data are shown for one of the training/testing rounds. cAβ+ , correctly classified Aβ+ (true positive; PET=Aβ+; model prediction=Aβ+); mAβ+ , misclassified Aβ+ (false negative; PET=Aβ+; model prediction=Aβ–); cAβ–, correctly classified Aβ– (true negative; PET=Aβ–; model prediction=Aβ–); mAβ–, misclassified Aβ– (false positive; PET=Aβ–; model prediction=Aβ+); FDG, ^{18}F-fluorodeoxyglucose PET; CSF Aβ, β-amyloid$_{1-42}$ in CSF; CSF p-tau, phosphorylated tau at the threonine 181 in CSF; * ** $p < 0.005$; * * $p < 0.01$; * $p < 0.05$.

positive individuals that provide enhanced information about amyloid pathology relative to morphometrics, such as cortical thickness and hippocampal volume, and are distinct from the effects of typical aging. The discussion primarily addressed findings from the PET dataset ($A\beta_{PET}$) analysis unless otherwise specified throughout the section because the extent and magnitude of effects were substantially smaller in the full sample ($A\beta_{PET-CSF}$).

Extensive effects were observed across the posterior temporal and parietal as well as medial prefrontal cortex, surprisingly consistent with the typical localization of amyloid PET signal (Buckner et al., 2005; Gonzalez-Escamilla et al., 2021) and with signal changes in AD reported in (Salat et al., 2011). It suggests that MSSM could provide a regional brain 'map' that is not available from systemic markers such as plasma markers. Combining multiscale scales, the MSSM procedure revealed stronger and more extensive effects compared to cortical thickness measurements alone. The MSSM features substantially increased the number of significant vertices statistically different in Aβ+ compared to Aβ– (both cognitively healthy). The regions most affected overlapped those known to show early and aggressive degeneration from pathology studies (Ball, 1978; Hyman et al., 2012) and included the entorhinal cortex, parahippocampal cortex, cingulate, precuneus, and temporal pole (see Fig. 4A, B). The effects also overlapped with Braak amyloid staging, potentially a Braak amyloid 'Stage 1′ or '2′ presentation (Nordberg, 2004). The MSSM signal was significantly correlated with amyloid PET signal in almost half of the brain cortex, much of which overlapped with regions where beta-amyloid accumulates and AD signature regions. Overall, these data suggest that the tissue signal properties could be a microstructural marker of pathologic mechanisms that are more preserved from cortical atrophy or that have a distinct longitudinal pattern in the disease process.

Among the MSSM feature set, the gray 60%/white 1.0 mm contrast measure emerged as the most sensitive component to group differences across the greatest percentage of vertices (35%). It is noteworthy that this feature, colored in orange in Fig. 5, is in AD signature regions and regions that accumulate amyloid (Figs. 4C, 4D). Combining across all contrast metrics (GWRs), GWRs were the dominating feature in 89% and cortical thickness in 11% of the total vertices. On the contrary, the cortical thickness component was the most sensitive when differentiating AD from CU, and it was the most important feature in 37% of the total vertices (Jang et al., 2022), suggesting that tissue contrast measures may be more sensitive than cortical thickness measures early in the course of AD. The laterality observed in amyloid effects is interesting to note because structural differences were more extensive in the left hemisphere than the right. This may be relevant to findings in adult lifespan studies (Roe et al., 2021) showing that changes in cortical thickness asymmetry are present in typical aging and accelerated in AD. Further study can investigate whether this laterality in the MSSM metrics is a generalizable feature in other samples.

We demonstrated that MSSM can differentiate unimpaired individuals with AD amyloid pathology using only a single standard structural MRI. This approach has been validated by PET imaging. The proposed MSSM biomarkers from a standard T1-weighted image increased sensitivity to structural differences between cognitively intact amyloid positive (Aβ+) individuals and precisely matched cognitively intact Aβ– controls. Thus, this procedure may provide a proxy metric for the 'A′ component as well as the 'N′ of the 'A-T-N′ biological framework for AD when molecular biomarkers are not available. These measures can be used independently or in a complementary manner to tau biomarkers to complete the 'A-T-N′ characterization of individual patients.

The MSSM features classified Aβ+ /– with significantly greater accuracy than standard measures of cortical thickness, hippocampal volume, or GWRs (see Table 3). More importantly, we learned from the ablation study that the intensity contrasts (i.e., GWRs) may contribute more than the conventional morphometry (i.e., cortical thickness) to detecting amyloid positive individuals. MSSM also outperformed previously reported models that used cognitive performance (both self-assessed and partner-assessed)(Albright et al., 2021), morphometric features from MRI (Ten Kate et al., 2018), clinical information (Tosun et al., 2021), and the combination of genetic, cognitive, and demographic features (Ansart et al., 2020; Michelle M Mielke et al., 2012). Only a couple of studies have reported comparable performance to ours to the best of our knowledge – i.e., a deep learning model that takes MRI

as input (Tosun et al., 2021) and a model combining and optimizing multiple cognitive scores that are sensitive to amyloid pathology (Hahn et al., 2020). Compared with the deep learning model, the proposed method requires much less computing resources and training time while providing improved explainability. Since we had cognitively matched sample, chances are low to achieve comparable classification performance using combined cognitive scores in this dataset. We improved our prior implementation by optimizing the number of vertices to be fed into the model, thereby enabling two-way dimensionality reduction, first along the feature type dimension and second along the spatial dimension. However, we still observe some degree of overfitting; hence one of the next steps is to further improve the model with a larger, more variable sample and use data augmentation techniques. Misclassified individuals provide interesting next steps to improve the accuracy of our MSSM amyloid classification. For example, adding demographic features to MSSM did not enhance performance in this sample, which implies that the MSSM features capture the variance of the demographic features or that classification performance has reached a ceiling. However, certain demographic factors such as age differed in the misclassified sample. This suggests that more expansive training models including a wider age range may improve classification performance. Additionally, misclassified Aβ+ individuals exhibited very interesting patterns when examined in detail. For example, although they were Aβ+ *and* older than correctly classified Aβ+ , their brain structural measures were 'healthier' (or matched) to the other groups (e.g., similar entorhinal volume to the other groups and reduced ventricular volumes even though they were older than the correctly classified sample). The β-amyloid status measured in cortical regions with PET, which was used as ground truth in this study, was not always consistent with β-amyloid in CSF. The CSF measure may become abnormal prior to PET, and this may explain some misclassifications. Counterintuitively, although the brains seemed healthier from a structural perspective, FDG was reduced in the misclassified Aβ+ individuals, suggesting some degree of metabolic dysfunction. Overall, these data suggest that misclassified Aβ+ individuals may represent a unique group of individuals, potentially exhibiting some form of cognitive resilience in the face of aging and AD pathology and possibly related to preserved brain structure (Bocancea et al., 2021; Chételat et al., 2010; Stern et al., 2020).

Regions showing effects of amyloid were substantially smaller in the $A\beta_{PET-CSF}$ dataset compared to the $A\beta_{PET}$ dataset even though the sample size was twice that of $A\beta_{PET}$. The classification performance also dropped compared to when the main dataset was used, suggesting that ambiguity exists in defining the ground truth when merging amyloid PET and CSF measures and that individuals around the positivity cutoff are difficult to be classified. This is likely because amyloid plaques are the gradual buildup and accumulation of protein fragments between neurons over many years, meaning that no clear boundary exists between amyloid positivity and negativity. Also, combining of datasets with different type of amyloid measures may have induced noise around the cutoff values for positivity because the PET and CSF measures do not necessarily agree to each other.

While current classification performance may not yet meet clinical application standards, these advancements will have potential relevance for screening for preclinical AD in clinical trials, as the MSSM technique requires only a single T1-weighted MRI. Ongoing groundbreaking trials (e.g., The A4 Study https://a4study.org/) have performed PET imaging in large samples to determine amyloid positivity prior to enrollment. T1-weighted MRI, which is widely available, relatively low cost, and noninvasive, could be used as an initial screen for likely PET amyloid positivity and then confirmed with the gold standard assessment. For example, if we assume that an institution aims to recruit 30 individuals that are Aβ positive for a trial, MSSM-based prescreening using either existing data or new MR imaging could significantly reduce costs for screening the individuals with Aβ+ . Moreover, the MRI session also offers the opportunity to identify cerebrovascular or other lesions that may be exclusionary from other sequences. The following is an example of cost calculation when MSSM is used for prescreening. Assume that the group recruits adults older than 60 years old and around 30% of the population are Aβ positive (Jansen et al., 2022) and that costs for clinical amyloid PET imaging and MR imaging are $4000 and $487, respectively. Since the precision of the MSSM for Aβ positivity is 69% (from the $A\beta_{PET-CSF}$ analysis) and the target count is 30, about 43 individuals need to be identified at prescreening who are likely Aβ+ . The institution would need to run MRI prescreening for roughly 143 individuals to identify 43 who are likely Aβ positive. Hence, the costs for PET imaging and MR imaging would be 43 x $4000 and 143 x $487, respectively, which sums to around $242,000. When there is no prescreening, they would need about 100 PET scans to recruit 30 Aβ+ , which would cost approximately $400,000. Therefore, they would save $138,000, or 34.5% of the original cost, in screening 30 individuals with amyloid positivity. In the calculation, the cost of an MRI is based on the price set by the Centers for Medicare & Medicaid Services (CMS) for clinical exams ("Medicare.gov Procedure Price Lookup for Outpatient Services," n.d.). Amyloid PET is currently not covered by Medicare for clinical care; hence the estimated research cost at the authors' hospital was used. Note that it can cost more for clinical exams (Andersen et al., 2021; Hellmuth et al., 2018; Tasakis and Tsolaki, 2015). Future work will further validate the MSSM procedure to avoid potential bias in recruitment.

To date, very few studies have used structural imaging robustly in the classification of amyloid or tau pathology in cognitively unimpaired individuals (Ten Kate et al., 2018; Tosun et al., 2021). There are many potential reasons including the following: a) structural changes in cognitively intact individuals are subtle, hard to detect, and not captured enough by morphometry such as cortical thickness, hippocampal volume, and ventricular volume (sample images are shown in Fig. S2), b) there exist many kinds of imaging hardware and software (both for MRI and PET) and this variability in imaging makes it hard to develop a generalizable model, c) training a model that detects a subtle difference from heterogeneous data requires a large dataset, however, collecting PET or CSF data from many unimpaired individuals may raise ethical concerns because PET is radioactive and CSF exams are invasive. The current study could help alleviate these ethical risks in clinical research by using the MSSM procedure for prescreening, which can substantially reduce the number of participants taking PET or CSF exams. We came up with strategies to tackle the first two difficulties by using highly localized normalization of tissue properties and combining it with morphometry, thereby making the procedure more generalizable. Also, various data were included in training in multiple aspects for further generalizability – e.g., 62 imaging sites, 3 MRI manufacturers, 15 MRI models, 2 kinds of MRI field strength, 3 PET manufacturers, 19 PET models, mildly varying imaging parameters, and a wide range of demographic characteristics. Nevertheless, we still observed regional difference between scanners (especially the MR manufacturers) in terms of the GM/WM tissue contrast and the resultant MSSM signal, meaning there is still much room for improvement.

Additional studies are needed to further optimize the procedure for improved generalizability and determine the origin of misclassifications. Local samples are being collected for external validation of the MSSM procedure. An array of novel features can be added from MRI quantification, including surface area, gyrification index, and curvature, to further improve the performance. Given the current results showing similar patterns to a typical amyloid PET map, it will be a reasonable next step to investigate whether the MSSM features can be used to predict regional amyloid deposition. Although we argue that MSSM is likely detecting effects in regions high in amyloid, some regions are less conclusive and it might be detecting something other than amyloid in those regions (e.g., tissue changes secondary to amyloid or other processes). We only report associations here and hope to further investigate specificity in future work. The current study used ^{18}F-florbetapir PET imaging to determine amyloid positivity. Future studies will investigate whether MSSM can detect cognitively healthy individuals with tau

positivity, validated by ^{18}F-flortaucipir (AV-1451) PET imaging, or with amyloid positivity, validated by PET imaging with other tracers such as ^{18}F-florbetaben and ^{18}F-fluorodeoxyglucose (FDG) as well as individuals that show longitudinal cognitive decline. For the findings to be considered and applied in the clinic, we plan to validate the procedure on a clinical database with lower image quality (e.g., lower signal-to-noise ratio, lower image resolution) and participants of more diverse races and ethnicities. We do not know the exact mechanisms of MSSM yet, and there may be factors other than neurodegeneration that contribute to the effects measured (biological and technical). It is possible that patient motion contributes to the effects measured; however, it is unlikely that motion would show such a major differential impact on MSSM compared to cortical thickness. Future work in the Lifespan Human Connectome Project Aging study (HCP-A; https://www.humanconnectome.org/study/hcp-lifespan-aging)(Bookheimer et al., 2019; Harms et al., 2018; B. Li et al., 2021), where motion navigators were acquired, will allow us to examine this in detail. With these caveats, we conclude that the MSSM procedure can serve as more sensitive indicators of AD amyloid pathology and is preferable to morphometry alone.

CRediT authorship contribution statement

Jang Ikbeom: Writing – review & editing, Writing – original draft, Visualization, Validation, Software, Methodology, Investigation, Formal analysis, Data curation, Conceptualization. **Dickerson Bradford C.:** Writing – original draft, Funding acquisition. **Salat David H.:** Writing – review & editing, Writing – original draft, Supervision, Investigation, Funding acquisition, Conceptualization. **Jacoby John:** Visualization, Formal analysis. **Huang Susie Y.:** Writing – original draft. **Li Binyin:** Writing – original draft, Visualization. **Rashid Barnaly:** Writing – review & editing.

Funding

This work was funded by the National Institutes of Health (NIH) grant R21AG072431 and was made possible by the computational resources provided by NIH Shared Instrumentation Grants 1S10RR023401, 1S10RR019307, and 1S10RR023043. It was partially supported by Hankuk University of Foreign Studies Research Fund of 2023.

Declaration of Competing Interest

In the past 36 months, outside the submitted work, B.C.D has received research support from NIH; consulted for Acadia, Alector, Arkuda, Biogen, Denali, Lilly, Merck, Novartis, Takeda, and Wave LifeSciences; performed editorial duties with payment for Elsevier (Neuroimage: Clinical and Cortex); and received royalties from Oxford University Press and Cambridge University Press. D.H.S has held leadership or fiduciary role in Niji Corp, Smart Ion, and Salat Research Consulting; and performed editorial duties with payment for Elsevier (Neuroimage and Neurobiology of Aging). S.Y.H has received research support from NIH and Siemens Healthineers; and consulted for Siemens Healthineers. The other authors declare that they have no competing interests.

Acknowledgments

The authors would like to acknowledge the valuable consultation from Dr. Douglas Greve regarding visualization methods using FreeSurfer and the constructive feedback from our anonymous reviewers.

Data collection and sharing for ADNI in the study was funded by the Alzheimer's Disease Neuroimaging Initiative (ADNI) (National Institutes of Health Grant U01 AG024904) and DOD ADNI (Department of Defense award number W81XWH-12-2-0012). ADNI is funded by the National Institute on Aging, the National Institute of Biomedical Imaging and Bioengineering, and through generous contributions from the following: AbbVie, Alzheimer's Association; Alzheimer's Drug Discovery Foundation; Araclon Biotech; BioClinica, Inc.; Biogen; Bristol-Myers Squibb Company; CereSpir, Inc.; Cogstate; Eisai Inc.; Elan Pharmaceuticals, Inc.; Eli Lilly and Company; EuroImmun; F. Hoffmann-La Roche Ltd and its affiliated company Genentech, Inc.; Fujirebio; GE Healthcare; IXICO Ltd.; Janssen Alzheimer Immunotherapy Research & Development, LLC.; Johnson & Johnson Pharmaceutical Research & Development LLC.; Lumosity; Lundbeck; Merck & Co., Inc.; Meso Scale Diagnostics, LLC.; NeuroRx Research; Neurotrack Technologies; Novartis Pharmaceuticals Corporation; Pfizer Inc.; Piramal Imaging; Servier; Takeda Pharmaceutical Company; and Transition Therapeutics. The Canadian Institutes of Health Research is providing funds to support ADNI clinical sites in Canada. Private sector contributions are facilitated by the Foundation for the National Institutes of Health (www.fnih.org). The grantee organization is the Northern California Institute for Research and Education, and the study is coordinated by the Alzheimer's Therapeutic Research Institute at the University of Southern California. ADNI data are disseminated by the Laboratory for Neuro Imaging at the University of Southern California.

A. Additional descriptions

A.1. PLS regression

Let $\boldsymbol{Y}$ a matrix of size $N \times K$ where N observations are represented by K dependent variables. Let $\boldsymbol{X}$ a matrix of size $N \times F$ where F predictors are collected on the N observations. Here N is the number of participants, K is 1, and F is the number of feature maps in our case. Our goal is to fit a model that predicts $\boldsymbol{Y}$ (amyloid positivity in our problem) from $\boldsymbol{X}$ (a set of feature maps in our problem) and to describe their common structure. First, let $\boldsymbol{u}_1$ one column of $\boldsymbol{Y}$ or $\boldsymbol{y}$, and estimate $\boldsymbol{X}$ weights

$$\boldsymbol{w}_1 = \frac{\boldsymbol{X}^T\boldsymbol{u}_1}{\|\boldsymbol{X}^T\boldsymbol{u}_1\|}$$

and $\boldsymbol{X}$ factor scores

$$\boldsymbol{t}_1 = \boldsymbol{X}\boldsymbol{w}_1.$$

Then we estimate $\boldsymbol{Y}$ weights

$$\boldsymbol{q}_1 = \frac{\boldsymbol{u}_1^T\boldsymbol{t}_1}{\|\boldsymbol{u}_1^T\boldsymbol{t}_1\|},$$

and $\boldsymbol{Y}$ scores

$$\boldsymbol{u}_1 = \boldsymbol{Y}\boldsymbol{q}_1.$$

If $\boldsymbol{t}$ has not converged, go to eq. (1). If converged, continue to compute X loadings:

$$\boldsymbol{p}_1 = \frac{\boldsymbol{X}^T\boldsymbol{t}_1}{\boldsymbol{t}_1^T\boldsymbol{t}_1},$$

$$\boldsymbol{p}_{1,new} = \frac{\boldsymbol{p}_{1,old}}{\left\|\boldsymbol{p}_{1,old}\right\|},$$

$$\boldsymbol{t}_{1,new} = \boldsymbol{t}_{1,old}\left\|\boldsymbol{p}_{1,old}\right\|,$$

and

$$\boldsymbol{w}_{1,new} = \boldsymbol{w}_{1,old}\left\|\boldsymbol{p}_{1,old}\right\|.$$

The regression coefficient is found by:

$$b_1 = \frac{\boldsymbol{u}_1^T\boldsymbol{t}_1}{\boldsymbol{t}_1^T\boldsymbol{t}_1}.$$

After calculating scores and loadings for the first latent variable, the residuals of $\boldsymbol{X}$ and $\boldsymbol{Y}$ are calculated:

$$\boldsymbol{E}_1 = \boldsymbol{X} - \boldsymbol{t}_1\boldsymbol{p}_1^T$$

$$\boldsymbol{F}_1 = \boldsymbol{Y} - \boldsymbol{u}_1\boldsymbol{q}_1^T$$

We repeat these procedures while replacing $\boldsymbol{X}$ and $\boldsymbol{Y}$ with their residuals. Eventually, the PLS model is described as:

$$\boldsymbol{X} = \boldsymbol{T}\boldsymbol{P}^T + \boldsymbol{E}$$

and

$$\boldsymbol{Y} = \boldsymbol{U}\boldsymbol{Q}^T + \boldsymbol{F}.$$

A.2. Determining Cutoffs for Clear Positive and Negative Cases of Preclinical Amyloid Pathology

We fit a Gaussian mixture model with three components while allowing each component to have its general covariance matrix. The model weights were initialized using K-means clustering, and the expectation-maximization iterations ran up to 200 times. $\mu_{GM1} + 0.5\sigma_{GM1}$ was used for the upper bound of the amyloid negativity (i.e., $A\beta^-_{PET} < \mu_{GM1} + 0.5\sigma_{GM1}$) and $\mu_{GM3} + 0.5\sigma_{GM3}$ was used for the lower bound of the amyloid positivity (i.e., $A\beta^+_{PET} > \mu_{GM3} + 0.5\sigma_{GM3}$), where $A\beta^-_{PET}$ and $A\beta^+_{PET}$ denote the average florbetapir SUVR for each individual in the amyloid-negative and the amyloid-positive groups, respectively. μ_i and σ_i denote the mean and standard deviation of component $i \in \{GM1, GM2, GM3\}$, and $\mu_{GM1} < \mu_{GM2} < \mu_{GM3}$. As a result, individuals with an average florbetapir SUVR greater than 1.19 were considered amyloid-positive and amyloid-negative if lower than 1.05. We had this buffer in the amyloid positivity criteria to prevent mislabels that can be caused by using data collected with numerous PET manufacturers and scanner models as well as different imaging sites and ADNI phases/protocols.

Appendix A. Supporting information

Supplementary data associated with this article can be found in the online version at doi:10.1016/j.neurobiolaging.2024.01.005.

References

Albright, J., Ashford, M.T., Jin, C., Neuhaus, J., Rabinovici, G.D., Truran, D., Maruff, P., Mackin, R.S., Nosheny, R.L., Weiner, M.W., 2021. Machine learning approaches to predicting amyloid status using data from an online research and recruitment registry: the brain health registry. Alzheimer's Dement. Diagn. Assess. Dis. Monit. 13, 1–12. https://doi.org/10.1002/dad2.12207.

Allison, S.L., Koscik, R.L., Cary, R.P., Jonaitis, E.M., Rowley, H.A., Chin, N.A., Zetterberg, H., Blennow, K., Carlsson, C.M., Asthana, S., Bendlin, B.B., Johnson, S.C., 2019. Comparison of different MRI-based morphometric estimates for defining neurodegeneration across the Alzheimer's disease continuum. NeuroImage Clin. 23, 101895 https://doi.org/10.1016/j.nicl.2019.101895.

Andersen, E., Casteigne, B., Chapman, W.D., Creed, A., Foster, F., Lapins, A., Shatz, R., Sawyer, R.P., 2021. Diagnostic biomarkers in Alzheimer's disease. Biomark. Neuropsychiatry 5, 100041. https://doi.org/10.1016/J.BIONPS.2021.100041.

Ansart, M., Epelbaum, S., Gagliardi, G., Colliot, O., Dormont, D., Dubois, B., Hampel, H., Durrleman, S., 2020. Reduction of recruitment costs in preclinical AD trials: validation of automatic pre-screening algorithm for brain amyloidosis. Stat. Methods Med. Res. 29, 151–164. https://doi.org/10.1177/0962280218823036.

Ball, M.J., 1978. Topographic distribution of neurofibrillary tangles and granulovacuolar degeneration in hippocampal cortex of aging and demented patients. A quantitative study. Acta Neuropathol. 42, 73–80. https://doi.org/10.1007/BF00690970.

Bateman, R.J., Xiong, C., Benzinger, T.L.S., Fagan, A.M., Goate, A., Fox, N.C., Marcus, D. S., Cairns, N.J., Xie, X., Blazey, T.M., Holtzman, D.M., Santacruz, A., Buckles, V., Oliver, A., Moulder, K., Aisen, P.S., Ghetti, B., Klunk, W.E., McDade, E., Martins, R. N., Masters, C.L., Mayeux, R., Ringman, J.M., Rossor, M.N., Schofield, P.R., Sperling, R.A., Salloway, S., Morris, J.C., 2012. Clinical and biomarker changes in dominantly inherited Alzheimer's disease. N. Engl. J. Med. 367, 795–804. https://doi.org/10.1056/NEJMOA1202753.

Belathur Suresh, M., Fischl, B., Salat, D.H., 2018. Factors influencing accuracy of cortical thickness in the diagnosis of Alzheimer's disease. Hum. Brain Mapp. 39, 1500–1515. https://doi.org/10.1002/hbm.23922.

Bocancea, D.I., van Loenhoud, A.C., Groot, C., Barkhof, F., van der Flier, W.M., Ossenkoppele, R., 2021. Measuring resilience and resistance in aging and Alzheimer disease using residual methods. Neurology 97, 474–488. https://doi.org/10.1212/WNL.0000000000012499.

Bookheimer, S.Y., Salat, D.H., Terpstra, M., Ances, B.M., Barch, D.M., Buckner, R.L., Burgess, G.C., Curtiss, S.W., Diaz-Santos, M., Elam, J.S., Fischl, B., Greve, D.N., Hagy, H.A., Harms, M.P., Hatch, O.M., Hedden, T., Hodge, C., Japardi, K.C., Kuhn, T. P., Ly, T.K., Smith, S.M., Somerville, L.H., Uğurbil, K., van der Kouwe, A., Van Essen, D., Woods, R.P., Yacoub, E., 2019. The lifespan human connectome project in aging: an overview. NeuroImage 185, 335–348. https://doi.org/10.1016/j.neuroimage.2018.10.009.

Bucci, M., Chiotis, K., Nordberg, A., 2021. Alzheimer's disease profiled by fluid and imaging markers: tau PET best predicts cognitive decline. Mol. Psychiatry 26, 5888–5898. https://doi.org/10.1038/s41380-021-01263-2.

Buchhave, P., Minthon, L., Zetterberg, H., Wallin, Å.K., Blennow, K., Hansson, O., 2012. Cerebrospinal fluid levels ofβ-amyloid 1-42, but not of Tau, are fully changed already 5 to 10 years before the onset of Alzheimer dementia. Arch. Gen. Psychiatry 69, 98–106. https://doi.org/10.1001/ARCHGENPSYCHIATRY.2011.155.

Buckner, R.L., Snyder, A.Z., Shannon, B.J., LaRossa, G., Sachs, R., Fotenos, A.F., Sheline, Y.I., Klunk, W.E., Mathis, C.A., Morris, J.C., Mintun, M.A., 2005. Molecular, structural, and functional characterization of Alzheimer's disease: evidence for a relationship between default activity, amyloid, and memory. J. Neurosci. 25, 7709–7717. https://doi.org/10.1523/JNEUROSCI.2177-05.2005.

Camus, V., Payoux, P., Barré, L., Desgranges, B., Voisin, T., Tauber, C., La Joie, R., Tafani, M., Hommet, C., Chételat, G., Mondon, K., De La Sayette, V., Cottier, J.P., Beaufils, E., Ribeiro, M.J., Gissot, V., Vierron, E., Vercouillie, J., Vellas, B., Eustache, F., Guilloteau, D., 2012. Using PET with 18F-AV-45 (florbetapir) to quantify brain amyloid load in a clinical environment. Eur. J. Nucl. Med. Mol. Imaging 39, 621–631. https://doi.org/10.1007/S00259-011-2021-8/TABLES/4.

Chételat, G., Villemagne, V.L., Pike, K.E., Baron, J.C., Bourgeat, P., Jones, G., Faux, N.G., Ellis, K.A., Salvado, O., Szoeke, C., Martins, R.N., Ames, D., Masters, C.L., Rowe, C. C., 2010. Larger temporal volume in elderly with high versus low beta-amyloid deposition. Brain 133, 3349–3358. https://doi.org/10.1093/BRAIN/AWQ187.

Cho, Y., Seong, J.-K., Jeong, Y., Shin, S.Y., 2012. Individual subject classification for Alzheimer's disease based on incremental learning using a spatial frequency representation of cortical thickness data. NeuroImage 59, 2217–2230. https://doi.org/10.1016/j.neuroimage.2011.09.085.

Choi, B.-K., Madusanka, N., Choi, H.-K., So, J.-H., Kim, C.-H., Park, H.-G., Bhattacharjee, S., Prakash, D., 2020. Convolutional neural network-based MR image analysis for Alzheimer's disease classification. Curr. Med. Imaging Former. Curr. Med. Imaging Rev. 16, 27–35. https://doi.org/10.2174/1573405615666191021123854.

Dale, A.M., Fischl, B., Sereno, M.I., 1999. Cortical surface-based analysis: I. Segmentation and surface reconstruction. NeuroImage 9, 179–194. https://doi.org/10.1006/NIMG.1998.0395.

Davatzikos, C., Fan, Y., Wu, X., Shen, D., Resnick, S.M., 2008. Detection of prodromal Alzheimer's disease via pattern classification of magnetic resonance imaging. Neurobiol. Aging 29, 514–523. https://doi.org/10.1016/J.NEUROBIOLAGING.2006.11.010.

Desikan, R.S., Cabral, H.J., Hess, C.P., Dillon, W.P., Glastonbury, C.M., Weiner, M.W., Schmansky, N.J., Greve, D.N., Salat, D.H., Buckner, R.L., Fischl, B., Initiative, A.D.N., 2009. Automated MRI measures identify individuals with mild cognitive impairment and Alzheimer's disease. Brain 132, 2048–2057. https://doi.org/10.1093/BRAIN/AWP123.

Dumurgier, J., Schraen, S., Gabelle, A., Vercruysse, O., Bombois, S., Laplanche, J.L., Peoc'h, K., Sablonnière, B., Kastanenka, K.V., Delaby, C., Pasquier, F., Touchon, J., Hugon, J., Paquet, C., Lehmann, S., 2015. Cerebrospinal fluid amyloid-β 42/40 ratio in clinical setting of memory centers: a multicentric study. Alzheimer's Res. Ther. 7, 1–9. https://doi.org/10.1186/S13195-015-0114-5/FIGURES/3.

Ezzati, A., Harvey, D.J., Habeck, C., Golzar, A., Qureshi, I.A., Zammit, A.R., Hyun, J., Truelove-Hill, M., Hall, C.B., Davatzikos, C., Lipton, R.B., 2020. Predicting amyloid-β levels in amnestic mild cognitive impairment using machine learning techniques. J. Alzheimer's Dis.: JAD 73, 1211–1219. https://doi.org/10.3233/JAD-191038.

Fischl, B., Dale, A.M., 2000. Measuring the thickness of the human cerebral cortex from magnetic resonance images. Proc. Natl. Acad. Sci. 97, 11050–11055. https://doi.org/10.1073/pnas.200033797.

Fischl, B., Sereno, M.I., Dale, A.M., 1999a. Cortical surface-based analysis: II. Inflation, flattening, and a surface-based coordinate system. NeuroImage 9, 195–207. https://doi.org/10.1006/nimg.1998.0396.

Fischl, B., Sereno, M.I., Tootell, R.B.H., Dale, A.M., 1999b. High-resolution intersubject averaging and a coordinate system for the cortical surface. Hum. Brain Mapp. 8, 272–284. https://doi.org/10.1002/(SICI)1097-0193(1999)8:4<272::AID-HBM10>3.0.CO;2-4.

Fischl, B., Salat, D.H., Busa, E., Albert, M., Dieterich, M., Haselgrove, C., van der Kouwe, A., Killiany, R., Kennedy, D., Klaveness, S., Montillo, A., Makris, N., Rosen, B., Dale, A.M., 2002. Whole brain segmentation. Neuron 33, 341–355. https://doi.org/10.1016/S0896-6273(02)00569-X.

Fischl, B., van der Kouwe, A., Destrieux, C., Halgren, E., Ségonne, F., Salat, D.H., Busa, E., Seidman, L.J., Goldstein, J., Kennedy, D., Caviness, V., Makris, N., Rosen, B., Dale, A. M., 2004. Automatically parcellating the human cerebral cortex. Cereb. Cortex 14, 11–22. https://doi.org/10.1093/CERCOR/BHG087.

Fleisher, A.S., Chen, K., Liu, X., Roontiva, A., Thiyyagura, P., Ayutyanont, N., Joshi, A.D., Clark, C.M., Mintun, M.A., Pontecorvo, M.J., Doraiswamy, P.M., Johnson, K.A., Skovronsky, D.M., Reiman, E.M., 2011. Using positron emission tomography and florbetapir F 18 to image cortical amyloid in patients with mild cognitive impairment or dementia due to Alzheimer disease. Arch. Neurol. 68, 1404–1411. https://doi.org/10.1001/ARCHNEUROL.2011.150.

Gao, F., Yoon, H., Xu, Y., Goradia, D., Luo, J., Wu, T., Su, Y., 2020. AD-NET: age-adjust neural network for improved MCI to AD conversion prediction. NeuroImage Clin. 27, 102290 https://doi.org/10.1016/j.nicl.2020.102290.

Gonzalez-Escamilla, G., Miederer, I., Grothe, M.J., Schreckenberger, M., Muthuraman, M., Groppa, S., 2021. Metabolic and amyloid PET network reorganization in Alzheimer's disease: differential patterns and partial volume effects. Brain Imaging Behav. 15, 190–204. https://doi.org/10.1007/S11682-019-00247-9/FIGURES/5.

Hahn, A., Kim, Y.J., Kim, H.J., Jang, H., Cho, H., Choi, S.H., Kim, B.C., Park, K.W., Na, D. L., Chin, J., Seo, S.W., 2020. The preclinical amyloid sensitive composite to determine subtle cognitive differences in preclinical Alzheimer's disease. Sci. Rep. 10, 1–11. https://doi.org/10.1038/s41598-020-70386-3.

Hansson, O., Seibyl, J., Stomrud, E., Zetterberg, H., Trojanowski, J.Q., Bittner, T., Lifke, V., Corradini, V., Eichenlaub, U., Batrla, R., Buck, K., Zink, K., Rabe, C., Blennow, K., Shaw, L.M., 2018. CSF biomarkers of Alzheimer's disease concord with amyloid-β PETand predict clinical progression: a study of fully automated immunoassays in BioFINDER and ADNI cohorts. Alzheimer's Dement. 14, 1470–1481. https://doi.org/10.1016/J.JALZ.2018.01.010.

Harms, M.P., Somerville, L.H., Ances, B.M., Andersson, J., Barch, D.M., Bastiani, M., Bookheimer, S.Y., Brown, T.B., Buckner, R.L., Burgess, G.C., Coalson, T.S., Chappell, M.A., Dapretto, M., Douaud, G., Fischl, B., Glasser, M.F., Greve, D.N., Hodge, C., Jamison, K.W., Jbabdi, S., Kandala, S., Li, X., Mair, R.W., Mangia, S., Marcus, D., Mascali, D., Moeller, S., Nichols, T.E., Robinson, E.C., Salat, D.H., Smith, S.M., Sotiropoulos, S.N., Terpstra, M., Thomas, K.M., Tisdall, M.D., Ugurbil, K., van der Kouwe, A., Woods, R.P., Zöllei, L., Van Essen, D.C., Yacoub, E., 2018. Extending the human connectome project across ages: imaging protocols for the lifespan development and aging projects. NeuroImage 183, 972–984. https://doi.org/10.1016/j.neuroimage.2018.09.060.

Hellmuth, J., Milanini, B., Masliah, E., Tartaglia, M.C., Dunlop, M.B., Moore, D.J., Javandel, S., DeVaughn, S., Valcour, V., 2018. A neuropathologic diagnosis of Alzheimer's disease in an older adult with HIV-associated neurocognitive disorder. Neurocase 24, 213. https://doi.org/10.1080/13554794.2018.1530362.

Hyman, B.T., Phelps, C.H., Beach, T.G., Bigio, E.H., Cairns, N.J., Carrillo, M.C., Dickson, D.W., Duyckaerts, C., Frosch, M.P., Masliah, E., Mirra, S.S., Nelson, P.T., Schneider, J.A., Thal, D.R., Thies, B., Trojanowski, J.Q., Vinters, H.V., Montine, T.J., 2012. National Institute on aging-Alzheimer's association guidelines for the neuropathologic assessment of Alzheimer's disease. Alzheimer's Dement. 8, 1–13. https://doi.org/10.1016/j.jalz.2011.10.007.

Jack, C.R., Knopman, D.S., Jagust, W.J., Shaw, L.M., Aisen, P.S., Weiner, M.W., Petersen, R.C., Trojanowski, J.Q., 2010. Hypothetical model of dynamic biomarkers of the Alzheimer's pathological cascade. Lancet Neurol. 9, 119–128. https://doi.org/10.1016/S1474-4422(09)70299-6.

Jack, C.R., Vemuri, P., Wiste, H.J., Weigand, S.D., Lesnick, T.G., Lowe, V., Kantarci, K., Bernstein, M.A., Senjem, M.L., Gunter, J.L., Boeve, B.F., Trojanowski, J.Q., Shaw, L. M., Aisen, P.S., Weiner, M.W., Petersen, R.C., Knopman, D.S., Initiative, for the A.D. N, 2012. Shapes of the trajectories of 5 major biomarkers of Alzheimer disease. Arch. Neurol. 69, 856–867. https://doi.org/10.1001/ARCHNEUROL.2011.3405.

Jack, C.R., Knopman, D.S., Jagust, W.J., Petersen, R.C., Weiner, M.W., Aisen, P.S., Shaw, L.M., Vemuri, P., Wiste, H.J., Weigand, S.D., Lesnick, T.G., Pankratz, V.S., Donohue, M.C., Trojanowski, J.Q., 2013. Tracking pathophysiological processes in Alzheimer's disease: an updated hypothetical model of dynamic biomarkers. Lancet Neurol. 12, 207–216. https://doi.org/10.1016/S1474-4422(12)70291-0.

Jang, I., Li, B., Riphagen, J.M., Dickerson, B.C., Salat, D.H., 2022. Multiscale structural mapping of Alzheimer's disease neurodegeneration. NeuroImage: Clin. 33. https://doi.org/10.1016/j.nicl.2022.102948.

Janghel, R.R., Rathore, Y.K., 2021. Deep convolution neural network based system for early diagnosis of Alzheimer's disease. IRBM 42, 258–267. https://doi.org/10.1016/j.irbm.2020.06.006.

Jansen, W.J., Janssen, O., Tijms, B.M., Vos, S.J.B., Ossenkoppele, R., Visser, P.J., Aarsland, D., Alcolea, D., Altomare, D., Von Arnim, C., Baiardi, S., Baldeiras, I., Barthel, H., Bateman, R.J., Van Berckel, B., Binette, A.P., Blennow, K., Boada, M., Boecker, H., Bottlaender, M., Den Braber, A., Brooks, D.J., Van Buchem, M.A., Camus, V., Carill, J.M., Cerman, J., Chen, K., Chételat, G., Chipi, E., Cohen, A.D., Daniels, A., Delarue, M., Didic, M., Drzezga, A., Dubois, B., Eckerström, M., Ekblad, L.L., Engelborghs, S., Epelbaum, S., Fagan, A.M., Fan, Y., Fladby, T., Fleisher, A.S., Van Der Flier, W.M., Förster, S., Fortea, J., Frederiksen, K.S., Freund-Levi, Y., Frings, L., Frisoni, G.B., Fröhlich, L., Gabryelewicz, T., Gertz, H.J., Gill, K.D., Gkatzima, O., Gómez-Tortosa, E., Grimmer, T., Guedj, E., Habeck, C.G., Hampel, H., Handels, R., Hansson, O., Hausner, L., Hellwig, S., Heneka, M.T., Herukka, S.K., Hildebrandt, H., Hodges, J., Hort, J., Huang, C.C., Iriondo, A.J., Itoh, Y., Ivanoiu, A., Jagust, W.J., Jessen, F., Johannsen, P., Johnson, K.A., Kandimalla, R., Kapaki, E.N., Kern, S., Kilander, L., Klimkowicz-Mrowiec, A., Klunk, W.E., Koglin, N., Kornhuber, J., Kramberger, M.G., Kuo, H.C., Van Laere, K., Landau, S.M., Landeau, B., Lee, D.Y., De Leon, M., Leyton, C.E., Lin, K.J., Lleó, A., Löwenmark, M., Madsen, K., Maier, W., Marcusson, J., Marquié, M., Martinez-Lage, P., Maserejian, N., Mattsson, N., De Mendonça, A., Meyer, P.T., Miller, B.L., Minatani, S., Mintun, M.A., Mok, V.C.T., Molinuevo, J.L., Morbelli, S.D., Morris, J.C., Mroczko, B., Na, D.L., Newberg, A., Nobili, F., Nordberg, A., Olde Rikkert, M.G.M., De Oliveira, C.R., Olivieri, P., Orellana, A., Paraskevas, G., Parchi, P., Pardini, M., Parnetti, L., Peters, O., Poirier, J., Popp, J., Prabhakar, S., Rabinovici, G.D., Ramakers, I.H., Rami, L., Reiman, E.M., Rinne, J.O., Rodrigue, K.M., Rodríguez-Rodriguez, E., Roe, C.M., Rosa-Neto, P., Rosen, H.J., Rot, U., Rowe, C.C., Rüther, E., Ruiz, A., Sabri, O., Sakhardande, J., Sánchez-Juan, P., Sando, S.B., Santana, I., Sarazin, M., Scheltens, P., Schröder, J., Selnes, P., Seo, S.W., Silva, D., Skoog, I., Snyder, P.J., Soininen, H., Sollberger, M., Sperling, R.A., Spiru, L., Stern, Y., Stomrud, E., Takeda, A., Teichmann, M., Teunissen, C.E., Thompson, L.I., Tomassen, J., Tsolaki, M., Vandenberghe, R., Verbeek, M.M., Verhey, F.R.J., Villemagne, V., Villeneuve, S., Vogelgsang, J., Waldemar, G., Wallin, A., Wallin, Å. K., Wiltfang, J., Wolk, D.A., Yen, T.C., Zboch, M., Zetterberg, H., 2022. Prevalence estimates of amyloid abnormality across the Alzheimer disease clinical spectrum. JAMA Neurol. 79, 228–243. https://doi.org/10.1001/JAMANEUROL.2021.5216.

Jefferson, A.L., Gifford, K.A., Damon, S., Chapman, G.W., Liu, D., Sparling, J., Dobromyslin, V., Salat, D., 2015. Gray & white matter tissue contrast differentiates mild cognitive impairment converters from non-converters. Brain Imaging Behav. 9, 141–148. https://doi.org/10.1007/s11682-014-9291-2.

Landau, S.M., Mintun, M.A., Joshi, A.D., Koeppe, R.A., Petersen, R.C., Aisen, P.S., Weiner, M.W., Jagust, W.J., 2012. Amyloid deposition, hypometabolism, and longitudinal cognitive decline. Ann. Neurol. 72, 578–586. https://doi.org/10.1002/ANA.23650.

Landau, S.M., Breault, C., Joshi, A.D., Pontecorvo, M., Mathis, C.A., Jagust, W.J., Mintun, M.A., 2013a. Amyloid-β imaging with Pittsburgh compound B and florbetapir: comparing radiotracers and quantification methods. J. Nucl. Med. 54, 70–77. https://doi.org/10.2967/jnumed.112.109009.

Landau, S.M., Lu, M., Joshi, A.D., Pontecorvo, M., Mintun, M.A., Trojanowski, J.Q., Shaw, L.M., Jagust, W.J., 2013b. Comparing positron emission tomography imaging and cerebrospinal fluid measurements of β-amyloid. Ann. Neurol. 74, 826–836. https://doi.org/10.1002/ANA.23908.

Li, B., Jang, I., Riphagen, J., Almaktoum, R., Yochim, K.M., Ances, B.M., Bookheimer, S. Y., Salat, D.H., 2021. Identifying individuals with Alzheimer's disease-like brains based on structural imaging in the human connectome project aging cohort. Hum. Brain Mapp. 42, 5535–5546. https://doi.org/10.1002/HBM.25626.

Li, H.T., Yuan, S.X., Wu, J.S., Gu, Y., Sun, X., 2021. Predicting conversion from mci to ad combining multi-modality data and based on molecular subtype. Brain Sci. 11. https://doi.org/10.3390/brainsci11060674.

Lin, W., Tong, T., Gao, Q., Guo, D., Du, X., Yang, Y., Guo, G., Xiao, M., Du, M., Qu, X., 2018. Convolutional neural networks-based MRI image analysis for the Alzheimer's disease prediction from mild cognitive impairment. Front. Neurosci. 12, 1–13. https://doi.org/10.3389/fnins.2018.00777.

Lu, D., Popuri, K., Ding, G.W., Balachandar, R., Beg, M.F., 2018. Multimodal and multiscale deep neural networks for the early diagnosis of Alzheimer's disease using structural MR and FDG-PET images. Sci. Rep. 8, 5697. https://doi.org/10.1038/s41598-018-22871-z.

Magnin, B., Mesrob, L., Kinkingnéhun, S., Pélégrini-Issac, M., Colliot, O., Sarazin, M., Dubois, B., Lehéricy, S., Benali, H., 2009. Support vector machine-based classification of Alzheimer's disease from whole-brain anatomical MRI. Neuroradiology 51, 73–83. https://doi.org/10.1007/s00234-008-0463-x.

Medicare.gov Procedure Price Lookup for Outpatient Services [WWW Document], n.d. URL https://www.medicare.gov/procedure-price-lookup/cost/70553/ (accessed 8.24.22).

Mielke, Michelle M., Wiste, H.J., Weigand, S.D., Knopman, D.S., Lowe, V.J., Roberts, R. O., Geda, Y.E., Swenson-Dravis, D.M., Boeve, B.F., Senjem, M.L., Vemuri, P., Petersen, R.C., Jack, C.R., 2012. Indicators of amyloid burden in a population-based study of cognitively normal elderly. Neurology 79 (15), 1570. https://doi.org/10.1212/WNL.0B013E31826E2696.

Nordberg, A., 2004. PET imaging of amyloid in Alzheimer's disease. Lancet Neurol. 3, 519–527. https://doi.org/10.1016/S1474-4422(04)00853-1.

Park, J.E., Park, B., Kim, S.J., Kim, H.S., Choi, C.G., Jung, S.C., Oh, J.Y., Lee, J.-H., Roh, J.H., Shim, W.H., 2017. Improved diagnostic accuracy of Alzheimer's disease by combining regional cortical thickness and default mode network functional connectivity: validated in the Alzheimer's disease neuroimaging initiative set. Korean J. Radiol. 18, 983. https://doi.org/10.3348/kjr.2017.18.6.983.

Popuri, K., Ma, D., Wang, L., Beg, M.F., 2020. Using machine learning to quantify structural MRI neurodegeneration patterns of Alzheimer's disease into dementia score: Independent validation on 8,834 images from ADNI, AIBL, OASIS, and MIRIAD databases. Hum. Brain Mapp. 41, 4127–4147. https://doi.org/10.1002/hbm.25115.

Roe, J.M., Vidal-Piñeiro, D., Sørensen, Ø., Brandmaier, A.M., Düzel, S., Gonzalez, H.A., Kievit, R.A., Knights, E., Kühn, S., Lindenberger, U., Mowinckel, A.M., Nyberg, L., Park, D.C., Pudas, S., Rundle, M.M., Walhovd, K.B., Fjell, A.M., Westerhausen, R., Masters, C.L., Bush, A.I., Fowler, C., Darby, D., Pertile, K., Restrepo, C., Roberts, B., Robertson, J., Rumble, R., Ryan, T., Collins, S., Thai, C., Trounson, B., Lennon, K., Li, Q.X., Ugarte, F.Y., Volitakis, I., Vovos, M., Williams, R., Baker, J., Russell, A., Peretti, M., Milicic, L., Lim, L., Rodrigues, M., Taddei, K., Taddei, T., Hone, E., Lim, F., Fernandez, S., Rainey-Smith, S., Pedrini, S., Martins, R., Doecke, J., Bourgeat, P., Fripp, J., Gibson, S., Leroux, H., Hanson, D., Dore, V., Zhang, P., Burnham, S., Rowe, C.C., Villemagne, V.L., Yates, P., Pejoska, S.B., Jones, G., Ames, D., Cyarto, E., Lautenschlager, N., Barnham, K., Cheng, L., Hill, A., Killeen, N., Maruff, P., Silbert, B., Brown, B., Sohrabi, H., Savage, G., Vacher, M., 2021. Asymmetric thinning of the cerebral cortex across the adult lifespan is accelerated in Alzheimer's disease. Nat. Commun. 12, 1–11. https://doi.org/10.1038/s41467-021-21057-y.

Salat, D.H., Lee, S.Y., van der Kouwe, A.J., Greve, D.N., Fischl, B., Rosas, H.D., 2009. Age-associated alterations in cortical gray and white matter signal intensity and gray to white matter contrast. NeuroImage 48, 21–28. https://doi.org/10.1016/j.neuroimage.2009.06.074.

Salat, D.H., Chen, J.J., van der Kouwe, A.J., Greve, D.N., Fischl, B., Rosas, H.D., 2011. Hippocampal degeneration is associated with temporal and limbic gray matter/white matter tissue contrast in Alzheimer's disease. NeuroImage 54, 1795–1802. https://doi.org/10.1016/j.neuroimage.2010.10.034.

Ségonne, F., Dale, A.M., Busa, E., Glessner, M., Salat, D., Hahn, H.K., Fischl, B., 2004. A hybrid approach to the skull stripping problem in MRI. NeuroImage 22, 1060–1075. https://doi.org/10.1016/J.NEUROIMAGE.2004.03.032.

Sørensen, L., Igel, C., Pai, A., Balas, I., Anker, C., Lillholm, M., Nielsen, M., 2017. Differential diagnosis of mild cognitive impairment and Alzheimer's disease using structural MRI cortical thickness, hippocampal shape, hippocampal texture, and volumetry. NeuroImage Clin. 13, 470–482. https://doi.org/10.1016/j.nicl.2016.11.025.

Stern, Y., Arenaza-Urquijo, E.M., Bartrés-Faz, D., Belleville, S., Cantilon, M., Chetelat, G., Ewers, M., Franzmeier, N., Kempermann, G., Kremen, W.S., Okonkwo, O., Scarmeas, N., Soldan, A., Udeh-Momoh, C., Valenzuela, M., Vemuri, P., Vuoksimaa, E., Urquiljo, E.M.A., Cantillon, M., Clouston, S.A.P., Estanga, A., Gold, B., Habeck, C., Jones, R., Kochhann, R., Lim, Y.Y., Martínez-Lage, P., Morbelli, S., Okonkwo, O., Ossenkoppele, R., Pettigrew, C., Rosen, A.C., Song, X., Van Loenhoud, A.C., 2020. Whitepaper: defining and investigating cognitive reserve, brain reserve, and brain maintenance. Alzheimer's Dement. 16, 1305–1311. https://doi.org/10.1016/J.JALZ.2018.07.219.

Sturchio, A., Dwivedi, A.K., Young, C.B., Malm, T., Marsili, L., Sharma, J.S., Mahajan, A., Hill, E.J., Andaloussi, S.E.L., Poston, K.L., Manfredsson, F.P., Schneider, L.S., Ezzat, K., Espay, A.J., 2021. High cerebrospinal amyloid-β 42 is associated with normal cognition in individuals with brain amyloidosis. eClinicalMedicine 38, 100988. https://doi.org/10.1016/j.eclinm.2021.100988.

Suk, H.-I., Lee, S.-W., Shen, D., 2014. Hierarchical feature representation and multimodal fusion with deep learning for AD/MCI diagnosis. NeuroImage 101, 569–582. https://doi.org/10.1016/j.neuroimage.2014.06.077.

Tasakis, R.N.S., Tsolaki, M., 2015. Mitochondria pathogenesis and dysfunction in Alzheimer's disease. Hell. J. Nucl. Med. 18, 10.

Ten Kate, M., Redolfi, A., Peira, E., Bos, I., Vos, S.J.B., Vandenberghe, R., Gabel, S., Schaeverbeke, J., Scheltens, P., Blin, O., Richardson, J.C., Bordet, R., Wallin, A., Eckerstrom, C., Molinuevo, J.L., Engelborghs, S., Van Broeckhoven, C., Martinez-Lage, P., Popp, J., Tsolaki, M., Verhey, F.R.J.J., Baird, A.L., Legido-Quigley, C., Bertram, L., Dobricic, V., Zetterberg, H., Lovestone, S., Streffer, J., Bianchetti, S., Novak, G.P., Revillard, J., Gordon, M.F., Xie, Z., Wottschel, V., Frisoni, G., Visser, P. J., Barkhof, F., 2018. MRI predictors of amyloid pathology: results from the EMIF-AD multimodal biomarker discovery study. Alzheimer's Res. Ther. 10, 1–12. https://doi.org/10.1186/s13195-018-0428-1.

Tosun, D., Veitch, D., Aisen, P., Jack, C.R., Jagust, W.J., Petersen, R.C., Saykin, A.J., Bollinger, J., Ovod, V., Mawuenyega, K.G., Bateman, R.J., Shaw, L.M., Trojanowski, J.Q., Blennow, K., Zetterberg, H., Weiner, M.W., 2021. Detection of β-amyloid positivity in Alzheimer's Disease Neuroimaging Initiative participants with demographics, cognition, MRI and plasma biomarkers. Brain Commun. 3. https://doi.org/10.1093/braincomms/fcab008.

Westman, E., Muehlboeck, J.-S., Simmons, A., 2012. Combining MRI and CSF measures for classification of Alzheimer's disease and prediction of mild cognitive impairment conversion. NeuroImage 62, 229–238. https://doi.org/10.1016/j.neuroimage.2012.04.056.

Wolz, R., Julkunen, V., Koikkalainen, J., Niskanen, E., Zhang, D.P., Rueckert, D., Soininen, H., Lötjönen, J., 2011. Multi-method analysis of MRI images in early diagnostics of Alzheimer's disease. PLoS One 6, e25446. https://doi.org/10.1371/journal.pone.0025446.

Zhang, D., Wang, Y., Zhou, L., Yuan, H., Shen, D., 2011. Multimodal classification of Alzheimer's disease and mild cognitive impairment. NeuroImage 55, 856–867. https://doi.org/10.1016/j.neuroimage.2011.01.008.